Rationally designed solid sorbent electrolyte exhibits dual CO_2/H_2O sorption and enables full gas phase CO_2 reduction

Marieke S. van Leeuwen[a,b,c]* *Seger Witteveen*[a,b,c] *Guy Vereecke*[b] *Nina Plankensteiner*[b,c] *Martijn J.W. Blom*[b,c] *Philippe M. Vereecken*[b,a,c]*

[a]KU Leuven, Center for Membrane separations, Adsorption, Catalysis and Spectroscopy (cMACS), Celestijnenlaan 200F, 3001 Leuven, Belgium
[b]imec, Kapeldreef 75, 3001 Leuven, Belgium
[c]EnergyVille-Thor Park 8320, 3600 Genk, Belgium
Email Address: philippe.vereecken@imec.be

Keywords: *CO_2 reduction, CO_2 capture, power-to-molecules, integrated carbon capture and utilization, ionogel, nanocomposite*

Efficient CO_2 electrolysis hinges on high CO_2 availability and controlled water transport towards and away from the catalyst. Traditional methods, such as direct CO_2 supply in the gas form or using CO_2 sorbent liquid electrolytes face significant limitations. In this study, we present a pioneering approach using a rationally designed CO_2/H_2O sorbent composite electrolyte, enabling low-temperature aqueous CO_2 electroreduction without liquid catholyte nor anolyte. The development of a multi-functional electrolyte in the form of a solid sorbent ionogel is introduced in this work. This novel material is designed to perform several tasks at once, namely (1) ensuring ionic conductivity (1.5-3 mS/cm) in a solid material, thereby removing salt precipitation issues linked to liquid aqueous electrolytes, (2) serving as local CO_2 concentrator (0.03-0.13 mmol CO_2/g for P_{CO2} 0.1-1 bar at 30 °C) to pave the way for flue gas based feed streams at lower CO_2 partial pressures and (3) regulating water supply and removal (0.3-2.3 mmol H_2O/g range at 85 % relative humidity depending on degree of methyl functionalization), to prevent preferential hydrogen evolution. This work offers a proof-of-concept for full-vapor phase CO_2 reduction, where methyl-functionalization of an ionic liquid-silica nanocomposite enable to steer the selectivity from H_2 to CO production.

1 Introduction

Recent models and international reports [1] have shown that transitioning from fossil fuels to renewable resources alone will not be enough to contain global temperature rise. Consequently, carbon capture strategies are essential to meet ambitious goals like those of the European Green Deal, which aims for "no net emissions of greenhouse gases by 2050, with economic growth decoupled from resource use" [2]. The electrochemical reduction of CO_2 to valuable products presents an attractive alternative to traditional carbon capture solutions where the greenhouse gas is merely retained (e.g. Carbon Capture and Sequestration (CCS)).

Interest in the low temperature aqueous CO_2 Reduction Reaction (CO2RR) began to gain momentum in the 1980's, with foundational work on intermediates and pH effects by pioneer scientists such as Hori et al. [3, 4]. Since then, significant steps have been made towards industrialization, including the anticipated launch of the first commercial electrochemically produced Sustainable Aviation Fuel plant in early 2025 [5]. However, to enable widespread industrialization of the electrochemical CO_2 reduction process, major advancements are still required, particularly in overcoming mass transport limitations of CO_2 in aqueous media.

Electrode and cell design are crucial to improve reactant supply to the electrode. Strategies have been developed to maximize the contact of reactants in a so-called triple phase boundary (3PB), where gas, ions and electrons meet for maximized reaction rate, which became crucial in achieving high CO_2 reduction partial current densities ($> 1\,A/cm^2$) [6]. Our literature search summarized in figure 1 shows that high-performance devices predominantly use gas-fed systems with porous cathode transport layers to enhance reactant supply. For this literature study, we have tabulated the cell types used in over 100 publications showing high CO_2 reduction performance over the past 5 years, defined as $> 0.1\,A/cm^2$, $> 50\,\%$ Faraday Efficiency towards CO_2 reduction products (as per the criteria selected previously by Vass and Staerz [7, 8]). The bibliography for this study is reported in the SI, section S.0. In such systems, CO_2 is typically

supplied in the gas phase and travels through a porous transport layer to meet the catalyst, which is in ionic contact with, for example, the liquid catholyte (*e.g,* in hybrid-type of cells, figure 1 right hand side).

The commercialization of hybrid cells is largely limited by the delicate pressure equilibrium across the electrode, leading to either flooding or drying out of the catalyst [9]. Moreover, this hydrophobicity of commonly used GDEs is altered by the reaction products and precipitation [10, 11]. In an attempt to address these issues, gas diffusion electrodes have been placed directly in contact with the membrane in Membrane Electrode Assemblies (figure 1, left). However, in both hybrid and MEA cells, the existence of a true 3PB has been questioned, and is in most cases more likely to be a two-phase boundary (2PB) where the CO_2 diffusion path is shortened over a thin liquid film at the catalyst [12, 13]. Key issues encountered in such systems include salt precipitation [14], lack of controlled H_2O and CO_2 transport to the catalyst [15], carbon loss due to membrane crossover [16] and stability of the catalyst and reaction environment [8, 17].

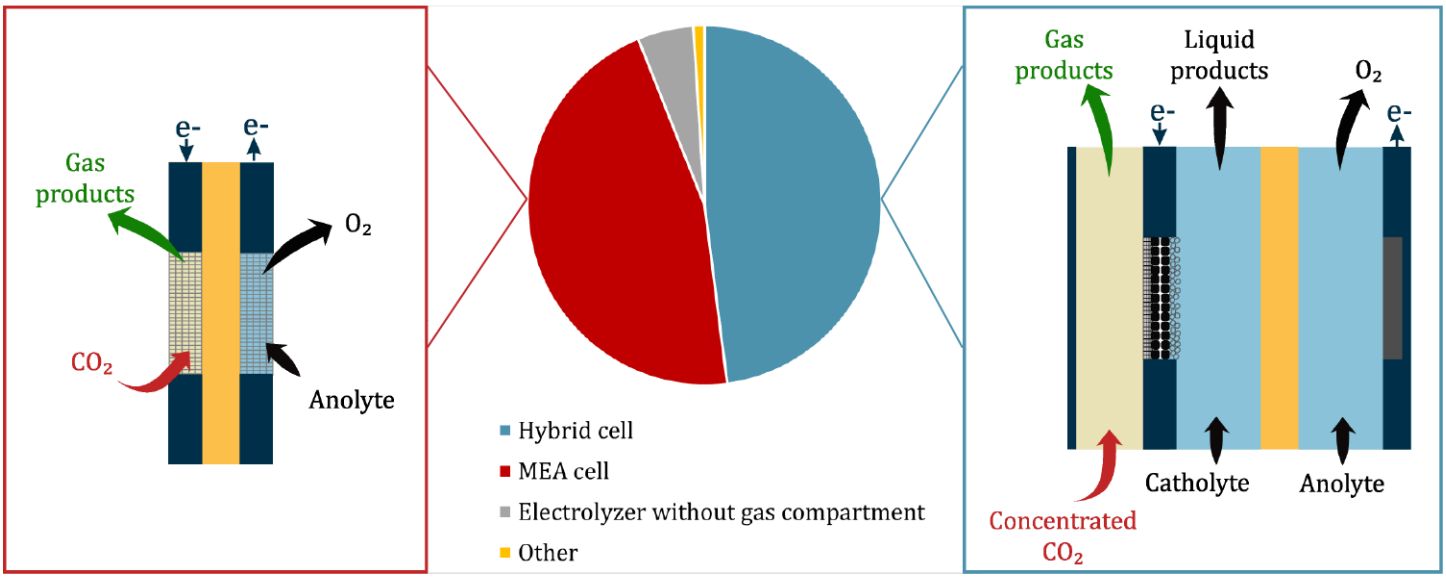

Figure 1: The two most common cell designs for high performance CO_2 electroreduction are(right) the hybrid cell, and (left) the Membrane Electrode Assembly cell. The distribution of the most reported cell types (center) is presented for high performance CO_2 reduction set-up, defined as $> 0.1\,A/cm^2$, $> 50\,\%$ Faraday Efficiency towards CO_2 reduction products by Vass and Staerz [7, 8]). The bibliography for this study is reported in the SI, section S.0.

This study introduces a novel concept and material to address the challenges faced by traditional GDEs, including limited reactant supply, cathodic flooding, pH control for selectivity, and salt precipitation. A Sorbent Composite Electrolyte (SCE) was designed, enabling full gas-phase CO_2 reduction, *i.e.,* in absence of liquid catholyte and anolyte. The SCE was designed to fulfill the roles of:

- CO_2 sorbent for local concentration increase,
- sink or source for the water involved in the electrochemical reaction,
- ionic conductor.

Rational design of an ionic liquid-silica nanocomposite enabled for the first time the demonstration of CO_2 electroreduction directly from a solid sorbent electrolyte using a fully gas phase feed. The affinity of the ionic liquid silica nanocomposites for CO_2 creates a CO_2-rich environment at the cathode [18], achieving ten times higher CO_2 concentrations than typical aqueous electrolytes. Functionalization of the silica network with methyl side-chains allowed tuning of the water uptake of the nanocomposite without affecting its CO_2 uptake.

To validate this novel concept, a dedicated and simplified test setup was developed, designed to isolate the core functionalities of the sorbent composite: CO_2 and H_2O uptake and transport, their electrochemical utilization from the sorbed phase, product release, and ionic conductivity. This setup intentionally avoids the complexity of practical electrolyzer architectures, found in MEAs or hybrid cells, where complex architectures and multiple components could obscure the origin of reactants or the source of ionic conduction. As an example, in such systems, it would be difficult to confirm whether CO_2 reduction occurred from the sorbent phase or from the gas-phase, or whether water and ions originated from the sorbent or from membrane crossover. Recent reports that integrate sorbents into highly engineered MEA-type electrolyzers often show current densities below what would be expected if the sorbent truly enhanced CO_2 availability compared to a "traditional" aqueous systems. This suggests that system-level limitations may mask the material's actual contribution. Therefore, in this work, we deliberately separate the material aspect from its integration, and focus on understanding the sorbent composite electrolyte from a materials perspective.

The SCE allowed uptake and reaction of both CO_2 and H_2O enabling for the first time low temperature CO_2 reduction from a sorbent in the absence of any liquid electrolyte. This foundational demonstration opens up a world of possibilities for novel MEA, electrolyzer cell, and stack designs, where sorbent-based electrolytes could be integrated into scalable architectures.

2 Effect of methyltrimethoxysilane addition on composite stability in water

The sorbent composite electrolytes were synthesized in a one-pot step via a non-hydrolytic sol-gel process described in the Experimental Section. The synthesized ionic liquid-silica nanocomposites can conceptually be described as a mesoporous silica matrix with high volumetric porosity ($\simeq 66\,\%$) encapsulating an ionic liquid [18, 19]. As explored in previous studies, a highly interconnected silica pore network results from the in-situ formation of the silica matrix. During the one-pot sol-gel process, all ionic liquid (1-butyl-1-methyl pyrrolidinium bis(trifluoro methylsulfonyl)imide ([BMP][TFSI])) is retained in the ionogel formed, thereby yielding a monolithic composite material.

Most [$TFSI^-$]-based ionogels are not stable in aqueous environments, as the affinity of the silica host matrix with water is usually higher than the host's affinity for the ionic liquid. Therefore, ionic liquid leaching is typically observed upon water immersion of the composites, and the latter was even reported as an effective ionic liquid recovery technique [20]. The addition of methyltrimethoxysilane (MTMS) to tetramethyl orthosilicate (TMOS) as silica precursor was reported by Néouze et al. to improve the water stability of [BMI][TFSI]-based composites [21]. In this work, a leaching test was established, similar to that reported by Horowitz et al. [20], to assess the stability of different ionogels in aqueous environments linked to the hydrophobicity of the silica network tuned by the addition of methyl groups.

[BMP][TFSI]-based nanocomposites were synthesized as described in the experimental section using tetraethyl orthosilicate (TEOS) as a silica precursor, and methyltrimethoxysilane (MTMS) to add methyl groups to the silica matrix (figure 2, right hand side), and thereby increase its hydrophobicity. Both the ionic liquid-to-silica molar ratio and the MTMS-to-TEOS molar ratio, *i.e.,* the amount of methyl groups on the silica network, were varied. A highly simplified vizualization of the nanocomposite components is proposed in figure 2, with on the left hand side, a non methyl modified silica network, formed from a TEOS-based sol-gel reaction. The [BMP][TFSI] molecular structure is provided below. On the right hand-side, the addition of methyl groups to the silica network when using a TEOS/MTMS-based sol-gel route is illustrated. The amount of ionic liquid leached after 24 hours of immersion in water was determined for nanocomposites sample using TGA and the percentage ionic liquid leached out is summarized in table 1 for different compositions. The details of the analysis can be found in the supporting information (S.2.1).

The addition of MTMS as complementary silica precursor has a strong effect on water stability, as it enables to prevent ionic liquid leaching. For 0.25 mol MTMS:mol TEOS, the leaching was reduced to approximately 50 %, compared to a complete loss of the ionic liquid (IL) in absence of MTMS. Leaching was prevented for nanocomposites with 1 mol MTMS:1 mol TEOS, which corresponds to a 12.5 % methylation of the silica. Decreasing the ionic liquid-to-silica molar ratio in absence of MTMS only resulted in a slight increase of ionic liquid leaching, and can be attributed to a higher affinity for water with increased silica

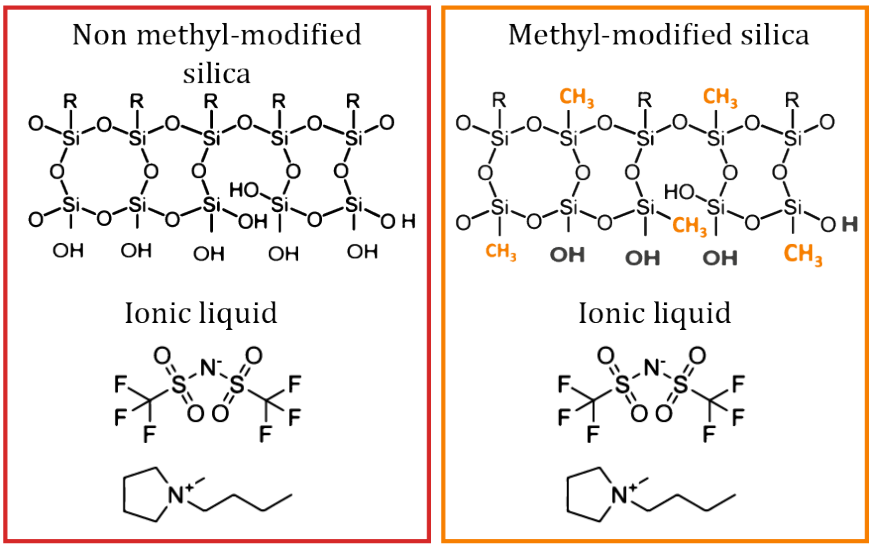

Figure 2: Conceptual vizualization of the (left) non methyl-modified silica network for [BMP][TFSI], HCOOH, and TEOS-based sol-gel synthesis, and (right) of the methyl-modified silica network for [BMP][TFSI], HCOOH, MTMS and TEOS-based sol-gel synthesis for a 1:1 MTMS:TEOS molar ratio.

content. Overall, addition of methyl groups by using a MTMS precursor enabled to significantly reduce the ionic liquid leaching in aqueous environment, and, for precursors with 1 mol MTMS: mol TEOS, to prevent ionic liquid loss for all ionic liquid/ silica compositions.

Table 1: Percentage leached ionic liquid (IL) for different [BMP][TFSI]-silica nanocomposites with different x (ionic liquid-to-silica molar ratio) and y (MTMS-to-TEOS precursor molar ratio).

x [mol IL: mol SiO_2]	y [mol MTMS: mol TEOS]	Ionic liquid leached [mass %]	x [mol IL: mol SiO_2]	y [mol MTMS: mol TEOS]	Ionic liquid leached [mass %]
0.5	0	**94**	1.5	0	**90**
0.5	0.25	**68**	1.5	0.25	**56**
0.5	1	**0**	1.5	1	**0**
1	0	**90**	2	0	**83**
1	0.25	**57**	2	0.25	**49**
1	1	**1.7**	2	1	**0**

3 Individual CO_2 and H_2O sorption properties

For low temperature CO_2 electroreduction, the sorbent composite electrolyte will require a plurality of functionalities. One of the main criteria is the ability of the material to provide a higher flux of reactants to catalyst sites than in systems operated with liquid electrolyte (H-cell or MEA with liquid anolyte, showcasing slight electrolyte permeation to the cathode). This is achieved by increasing hte CO_2 concentration in the material. Also, the water content in the nanocomposite will play an important role in steering the electroreduction reaction selectivity by controlling the CO_2 Reduction Reaction (CO2RR) versus the parasitic Hydrogen Evolution Reaction (HER) [22, 23]. Under an applied bias, and provided sufficient hydration, protons are expected to be the main ionic charge carriers given the typically negatively charged silica surface. Note that the bulky cations and anions of the ionic liquid can partly carry the ionic current but water and protons are needed to maintain reaction stoichiometry.

In previous work, we showed the CO_2 sorption properties of ionic liquid-silica nanocomposites in dry conditions [18], and demonstrated that at low partial pressures (< 0.4 bar), uptake is dominated by interfacial effects between the ionic liquid and the silica wall, while at higher pressures ($0.4 - 1$ bar), the contribution from the bulk ionic liquid confined in the pores becomes more significant. These findings

will now be extended to humidified environment. A few studies have reported on CO_2 uptake from ionic liquid-silica composites using humidified feeds, showing the displacement of CO_2 by water lowering the effective CO_2 concentration [24, 25, 26]. Interestingly, non-competitive CO_2/H_2O uptake was obtained by additional surface functionalization of the silica particles [27]. However, to our knowledge, no ionic liquid-silica nanocomposites were screened for both individual CO_2 and H_2O sorption, and for CO_2 sorption under varied H_2O content. In the following section, the CO_2 and H_2O sorption will be studied first individually, before being assessed under dynamic conditions.

3.1 CO_2 sorption

A screening method for CO_2 sorption via TGA was adapted from Chanut et al. [28], chosen for its accessibility and ease of implementation as a comparative tool across different sorbent compositions. A correction for buoyancy effects upon gas switching was applied as described in section 8 and validated for [BMP][TFSI] (SI, Figures S4–S5). As described in the methodology, the CO_2 uptake capacity was assessed at 0.1, 0.4, and 1 bar. After each TGA testing cycle, the material was regenerated, and the uptake at 0.4 bar was re-evaluated to confirm that no cycling history effects were present. The results obtained for the nanocomposites via the TGA method were benchmarked against previously reported adsorption isotherms [**?**], as shown in figure 3. The observed trends and order of magnitude are consistent across both methods, supporting the reliability of TGA for comparative screening.

Note that the absolute CO_2 uptake capacity values differ for both methods, TGA values being approximately 2.5 times lower at 1 bar CO_2 partial pressure. The difference in uptake values is expected and can be attributed to several factors. First, the experimental conditions differ significantly: adsorption isotherms begin from deep vacuum and gradually introduce CO_2, whereas TGA measurements start at atmospheric pressure under inert gas. This leads to different initial sample states and equilibrium conditions. Second, the temperature differs slightly (by 5 °C). Additionally, the measurement principles vary: TGA uses a spring-balance to track mass changes, while isotherms rely on pressure changes via manometry. The difference observed are in-line with variations observed for different reports of CO_2 uptake in ionic liquid depending on the study and method (± 60 % difference in CO_2 uptake [29]). Despite these differences, the TGA method shows low standard deviation across replicates (SI figure S5), indicating strong reproducibility. Moreover, sample-to-sample variability is limited, as evidenced by similar standard deviations for both nanocomposites and [BMP][TFSI] (SI **figure S5, S6**). These outcomes result from a thorough methodology development process, summarized in Table S5 (SI), which was designed to minimize systematic errors and enhance measurement robustness.

In summary, while absolute values differ due to inherent methodological contrasts, the TGA method provides a reliable and reproducible means for comparing CO_2 uptake across formulations. Its consistency with isotherm trends reinforces its value as a practical screening tool.

The CO_2 uptake measured by TGA was compared for three different ionic liquid-to-silica molar ratios under increasing partial pressure (figure 4). The left hand side picture shows the uptake for composites without methyl functionalization of the silica network, while the right hand side shows the uptake for nanocomposites with methyl groups, introduced using 1 mol MTMS:1 mol TEOS as precursor. Non-functionalized nanocomposites (figure 4a) showed unchanged CO_2 uptake for varied ionic liquid contents, which was previously observed from adsorption isotherms [18]. At lower CO_2 partial pressures (0-0.4 bar), interfacial effects between the silica and ionic liquid were postulated to influence sorption more than the bulk-like ionic liquid contained in the pores. Upon methylation of the silica network, no significant changes were observed in the CO_2 uptake, indicating that the addition of methyl groups does not impede the uptake of CO_2.

3.2 H_2O sorption

The water uptake in the nanocomposite was evaluated using TGA and the effect of silica content and its functionalization with hydrophobic methyl groups was assessed. Samples were saturated under high relative humidity (85 %) and subsequently heated to 150 °C (cf. section 8, Experimental Section). The

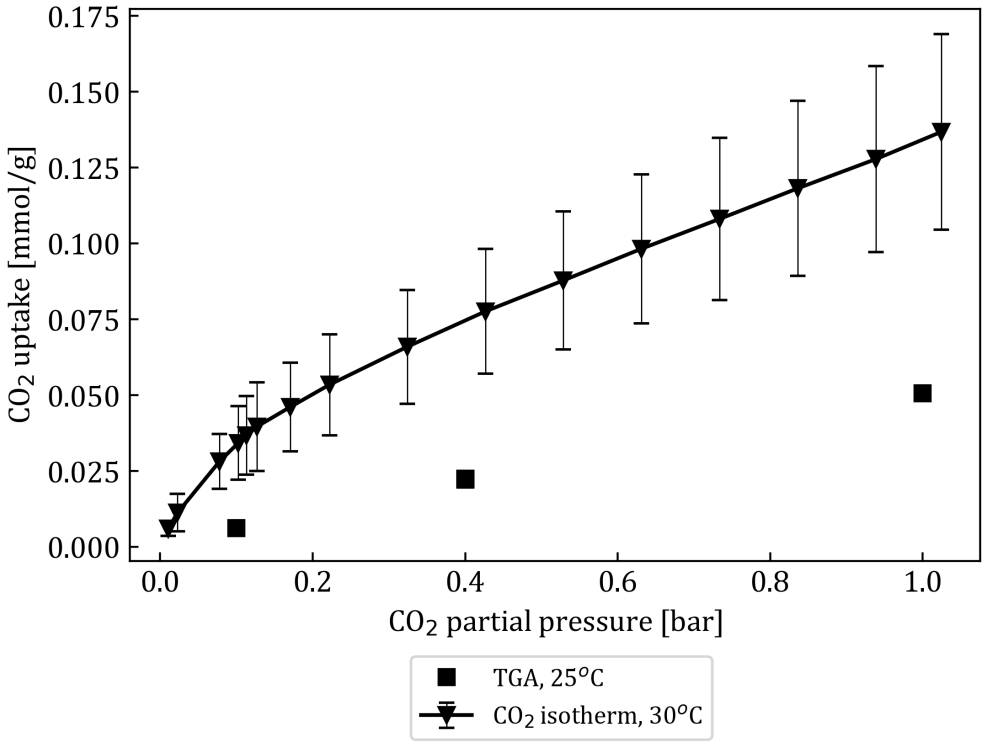

Figure 3: Comparison of the CO_2 uptake at different partial pressures for a silica-ionic liquid nanocomposite with x=2 mol IL: mol SiO_2, measured by TGA (■) with He as carrier gas, at a total gas flow rate of 25 mL/min, and measured by adsorption isotherm (▼).

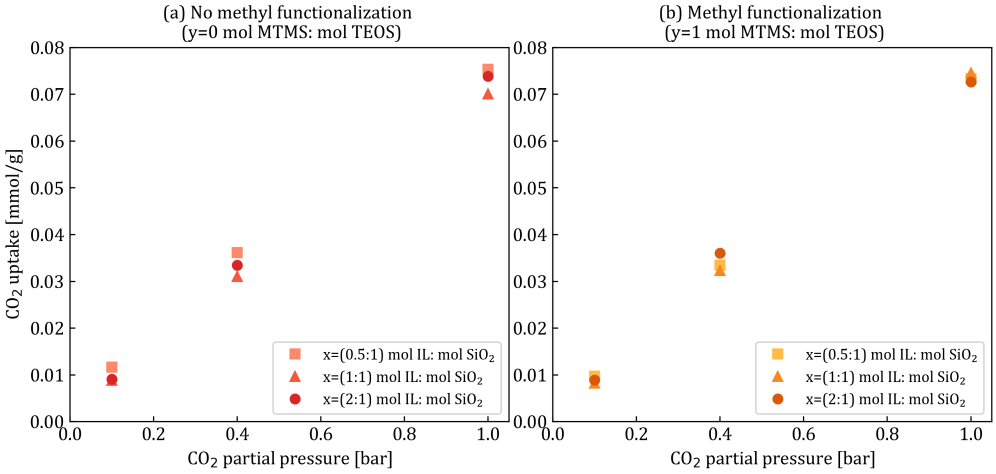

Figure 4: CO_2 uptake at different CO_2 partial pressures for [BMP][TFSI]-SiO_2 nanocomposites with x, the mol ionic liquid (IL): mol SiO_2 and y, the mol MTMS: mol TEOS used as precursor. Measurements were performed via TGA with He as carrier gas, at a total gas flow rate of 25 mL/min at 25 °C

.

mass loss between room temperature and 150 °C was attributed to water evaporation only as the composites are stable in this range, and from this, the water sorption was calculated. Water content is reported in figure 5 as a function of ionic liquid-to-silica molar ratio (x), for various amount of methyl-functionalization (MTMS:TEOS molar ratio, y). Overall, the water sorption capacity decreased for higher ionic liquid-to-silica ratios. Silica being a hygroscopic material, this finding is in-line with expectations. Addition of hydrophobic methyl groups to the silica network, *i.e.,* increasing y, the mol MTMS:mol TEOS precursor, resulted in a lowered water uptake as anticipated. By tuning the MTMS content, the water uptake of the nanocomposite can be controlled while keeping the CO_2 uptake unaffected.

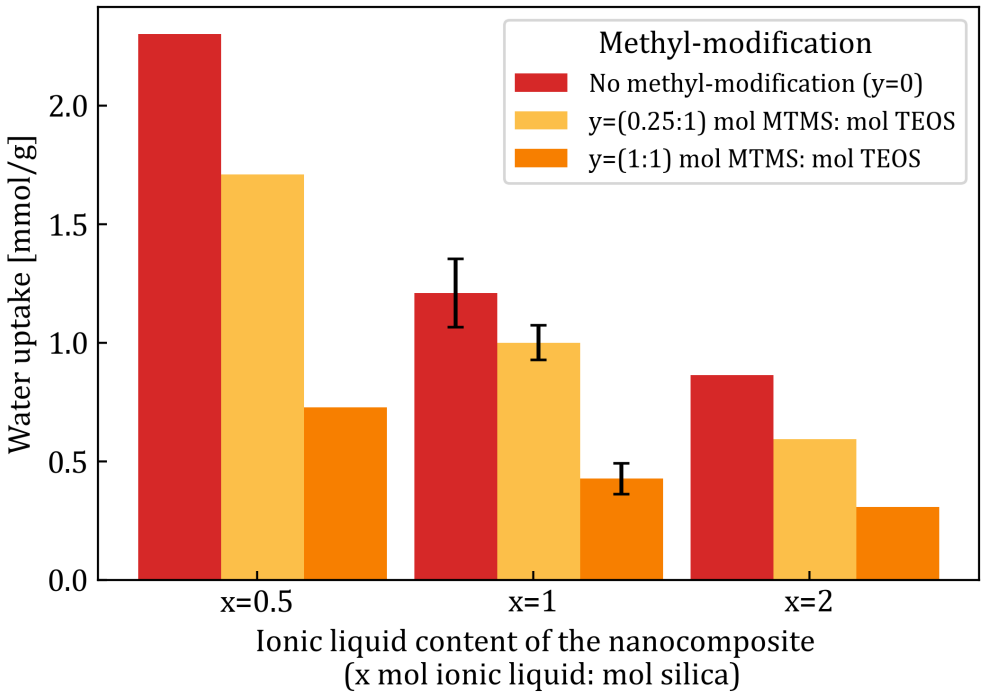

Figure 5: H_2O uptake of a [BMP][TFSI]-SiO_2 nanocomposite with x, the ionic liquid (IL)-to-silica molar ratio varied from x=0.5 to 2, and with varied methylation of the silica network (y=0, 0.25 and 1 mol MTMS: mol TEOS precursor), at 85 % relative humidity and 20 °C as measured by TGA by increasing temperature from 20 to 150 °C with ramp rate 1 °C/min under 25 mL/min nitrogen. Error bars for x = 1 mol IL:mol SiO_2 samples represent the standard deviation from three independent measurements on separately prepared samples.

4 Dynamic CO_2/H_2O measurements

4.1 Pellets

Dynamic conditions were used in order to properly assess the sorbent's performance of concurrent CO_2 and H_2O uptake and provide information about the competition between two sorbates and their possible displacement over time. The TGA method described by Chanut et al. [28] was used to evaluate the competitive H_2O and CO_2 uptake, as described in the experimental methods (section 8). Composites were saturated with H_2O at 85 % relative humidity prior to the measurement. The initial water content of the samples was taken from the average determined under section 3.2 for samples under similar water saturation conditions. Subsequent CO_2 sorption steps were performed, each separated by a drying step at higher temperature. The water evaporation for each step was determined as the mass loss over the heating step, and used to determine the post-heating water content.

The effect of both ionic liquid-to-silica ratio, x, and methyl functionalization of the silica wall, were investigated and are presented in figure 6. The CO_2 uptake at 1 bar and 298 K was determined as a function of water content in the composite and is represented from left to right for increasing methyl-functionalization of the silica (increasing y). In absence of MTMS precursor, *i.e.,* in absence of methyl groups on the silica matrix or $y = 0$ (figure 6a), a competition between CO_2 and H_2O can be seen. The CO_2 uptake indeed decreases linearly for higher water content, resulting in a negative slope, regardless of the ionic liquid-to-silica ratio x. A similar competition trend can be seen for MTMS-to-TEOS ratios of y=0.25 (figure 6b), with linear slopes in the same range as methyl-free (y=0) samples, ranging from -0.070 to -0.062 mol CO_2:H_2O. Interestingly, at the highest MTMS contents (y=1, figure 6c), the CO_2 uptake become nearly independent of the water content, with even flat slopes for x = 0.5 and 2 indicating non-competitive CO_2 and H_2O uptake in these cases.

Note that the maximum water content in figure 6 is lower than the saturation water content in figure 5. This is inherent to the measurement protocol as a long equilibration time of 3h is applied prior to the start

of the dynamic measurement with a first CO_2 exposure, which resulted in some water evaporation. Also, some slightly negative water contents are seen in figure 6, which are attributed to variations between the assumed initial water content (average from figure 5) and the actual water content in the sample. One could argue that the water content range is too small for the condition with high degree of methylation of the silica network (y=1) to claim independency. However, since the CO_2 uptake is in the same range as for lower methylation and low water content, it is safe to assume the CO_2 uptake remains constant regardless of the relative humidity.

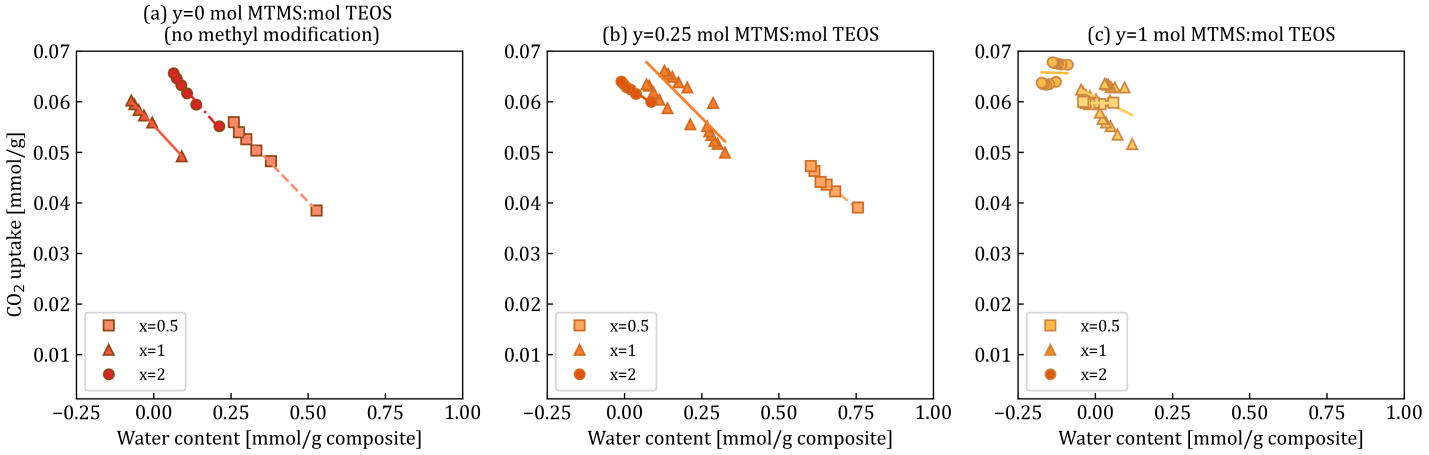

Figure 6: CO_2 uptake as a function of water content for silica-ionic liquid nanocomposites with different ionic liquid-to-silica molar ratios, denoted x, and varied degree of methylation (expressed as MTMS-to-TEOS molar ratios, denoted y). Measurements were performed via TGA with He as carrier gas, at a total gas flow rate of 25 mL/min. Results were corrected with an empty pan measurement to account for buoyancy effects of the pan volume, and corrected for the additional sample volume based on the sample density.

4.2 Translation to thin films

Upon integration of the sorbent in an electrochemical cell, thin layers will be required to ensure sufficient CO_2 diffusive flux over the solid material. However, translating material properties of the ionic liquid-silica gel from pellet to film is not trivial, as evaporation effects play an indisputably crucial role in sol-gel processes such as the one used for the nanocomposite fabrication [30]. The methodology for pellet synthesis was therefore used as starting point to explore properties of thin films with similar compositions. CO_2 and H_2O uptake, as well as their competition, were already evidenced in this work in pellet-form nanocomposites under humidified CO_2 feeds. These findings were enabled by adding MTMS to the TEOS precursor, which tuned and limited CO_2 displacement by water in humid conditions for molar ratios of 1:1 and ionic liquid-to-silica contents of 0.5 and 2.

4.2.1 Optimization of coating parameters

Conditions under which a gel is formed are known to impact the final material properties. The direct environment above the material, *e.g.,* the vapor pressure of solvents above the sol, will affect the evaporation rate and, among others, the porosity and interconnectedness of the silica network. Evidently, the sol is exposed to high solvent evaporation rates during spin-coating, on top of possible kinetic phase separation processes. To enable sufficient time for the non-hydrolytic hydroxylation prior to condensation and thus formation of the silica network, depositions were done when the sol viscosity reached more than double its initial value (*cf.* SI, figure S1). Due to the sudden gelation for MTMS-free samples, sols were cooled rapidly just before reaching the gel point, and spin-coated while cold, as described in more detail in the Materials and Methods section. MTMS-containing samples, on the other hand, required longer gel times, and were therefore kept for 8 hours at 25 °C prior to spin-coating. Note that nanocomposite coatings from MTMS-containing sols where the viscosity was less than double its initial value, yielded uptake properties

similar to coatings from MTMS-free sols, indicating that methyl groups were not incorporated into the silica network of the silica-ionic liquid nanocomposite.

4.2.2 Spectroscopic evidence of dynamic CO_2/H_2O uptake

The uptake of CO_2 and H_2O in thin films was studied using an ATR-FTIR flow cell set-up described in the Materials and Methods section. Samples were dried prior to testing, and loaded in the ATR-FTIR cell under dry N_2 flow. Differential spectra were then measured with respect to a background under N_2, firstly under CO_2, and secondly under humidified CO_2. Therefore, the spectra reported subsequently only showcase the apparition (or disappearing) of new peaks upon gas switching. The background spectra under inert gas, showing the presence of silica and [BMP][TFSI] ionic liquid, can be found in the supplementary information (figure S7, S8).

CO_2 in the gas form has four vibrational modes: symmetric and asymmetric stretching, and two degenerate bending modes. The asymmetric stretching ($\upsilon 3$) yields two peaks at 2337 and 2362 cm^{-1}, as illustrated from the differential ATR-FTIR spectrum in figure 7 of dry CO_2 gas (black dotted line), accounting for the P- and R-branches corresponding to the coupling of rotational-vibrational excitations [31].

Upon sorption in the nanocomposite, the asymmetric stretch signature changes shape, with a marked peak at the position of the previously defined P-branch, and a shoulder at lower frequencies (figure 7). This is in line with previous findings for CO_2 sorption in bulk ionic liquids [31, 32], with a Lorentzian type of peak and a shoulder approximately 12 cm^{-1} lower than the main adsorption peak [33]). The shoulder could be attributed to an anharmonic coupling of the asymmetric stretch and the thermally excited bending mode (expected aroung 670 cm^{-1}).

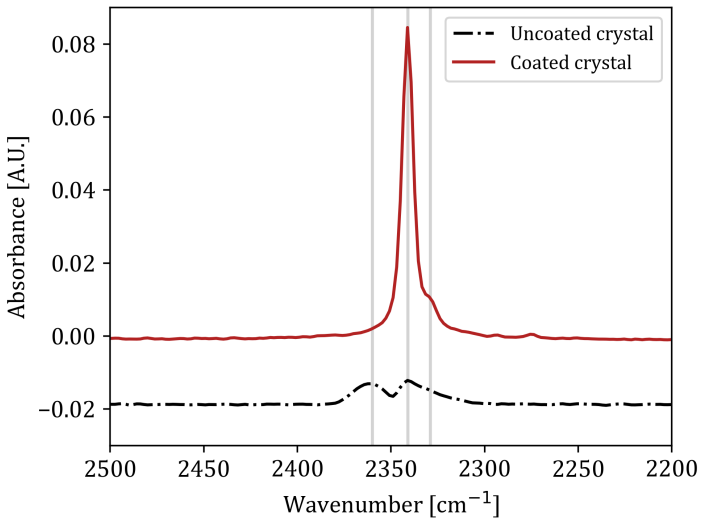

Figure 7: ATR-FTIR differential spectra for (black, −.) CO_2 gas and (red) adsorbed CO_2 under dry CO_2 flow with respect to a dry N_2 background for an uncoated FTIR crystal and coated crystal with a nanocomposite of ionic liquid-to-SiO_2 molar ratio x=1. The spectra are shifted with respect to one another for readability.

The possible displacement of CO_2 upon humidification was studied by following the CO_2 peak height after switching the feed stream from dry to humidified conditions. Two coatings with x = 2 mol ionic liquid: mol SiO_2 were evaluated, one with and one without methyl groups incorporated in the silica network. In both cases, the shape and position of the CO_2 peak described previously for sorbed CO_2 in the dry environment were maintained (figure 8). Uptake of free water in both coatings is apparent at 1643 cm^{-1} which is the characteristic bending vibration of "free water" [34]. Note that a free water signal is also present in the humidified CO_2 gas phase, albeit with smaller magnitude (figure 8 and SI Figure 4.8). The broad band around 3000-3750 cm^{-1} changed shape for the nanocomposites as compared to the humidified gas, but interestingly, also resulted in quite different shapes for the nanocomposites with and without methyl-groups in the silica network. The peaks in this range account for -OH related interactions mostly from adsorbed and free water. The adsorbed water is often indicated as ice-like water because of its immobile or solid nature

due to strong hydrogen bonding with silanol groups. The free water refers to non-hydrogen bonded water and is also indicated as liquid water. The liquid water asymmetric stretch in combination with bending vibration at 3404 cm^{-1} is shifted for the ice-like water asymmetric stretch to 3280 cm^{-1} [35, 36]. In the solid-state, H_2O molecules indeed form more hydrogen bonds, resulting in lower wavenumbers for the stretching vibrations upon immobilization. The ice-water peak is usually more pronounced for similar concentrations due to the augmented dipole. The apparition of additional peaks in the water 3000-3750 cm^{-1} region for nanocomposite coatings was attributed to SiOH termination interactions. Compared to humidified CO_2 in the gas phase, the humidified CO_2 absorbed in the nanocomposites show three additional peaks that can be attributed to interactions with the hygroscopic silica at 3000, 3540 and 3640 cm^{-1} [37]. The first weak shoulder can reflect interactions with the (a)symmetric fundamental stretching vibrations of $-CH_3$, *e.g.,* in the form of CH_3OH. The second is characteristic for water interactions with silanol groups through hydrogen bonding. The third can be attributed to vicinal SiOH stretching. Clearly, sorption of water in the silica-ionic liquid composites is obtained in different forms than water as available in the gas phase. The addition of methyl groups to the silica (orange) results in a lower ratio of solid and liquid-like water peaks compared to hydrated SiOH terminations, relative to non-functionalized silica. Overall, the quantitative H_2O uptake is lower than for the MTMS-free silica synthesis, in line with previous sorption experiments on pellets (figure 5).

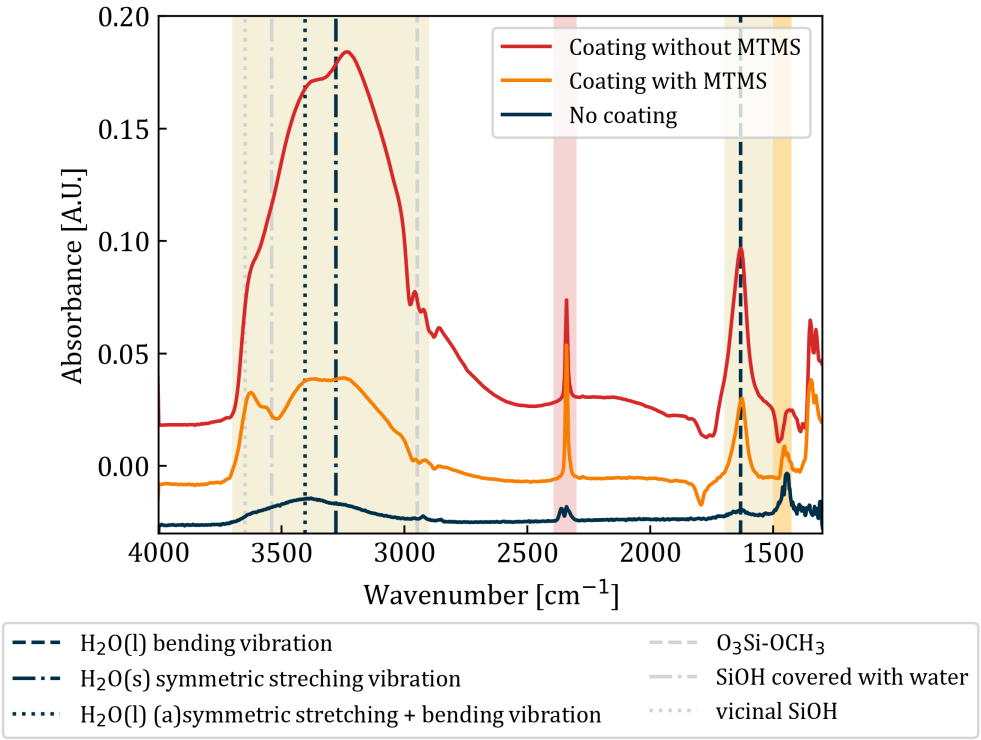

Figure 8: ATR-FTIR differential spectra under 100 mL/min humidified CO_2 feed with respect to a dry N_2 background for (dark blue) an uncoated FTIR crystal, (red) a methyl-free nanocomposite (x=2 mol [BMP][TFSI]:SiO_2), and (orange) a methyl-modified nanocomposite (x=2 mol [BMP][TFSI]:SiO_2, y=1 mol MTMS:TEOS). The regions in which H_2O sorption peaks are identified are shaded in light yellow, the regions in which CO_2 sorption peaks are identified are shaded in light red. The spectra are shifted with respect to one another for readability.

For the methyl-modified and non-modified coatings, the wet-to-dry CO_2 peak height ratio was computed from figure 9. For coatings synthesized in absence of MTMS, *i.e.,* without the incorporation of methyl groups to the silica network, a wet-to-dry CO_2 peak ratio of 0.71 was found, showing some competition between CO_2 and H_2O uptake, in line with the previous findings from TGA measurements for pellet nanocomposites. For methyl-modified silica coatings, with y, the TEOS-to-MTMS molar ratio, equal to 1, the wet-to-dry peak ratio increased to 0.94, showing nearly no displacement of CO_2 upon humidification of the stream. The non-displacement of CO_2 upon humidification was demonstrated for methyl-functionalized

pellets and thin film coatings.

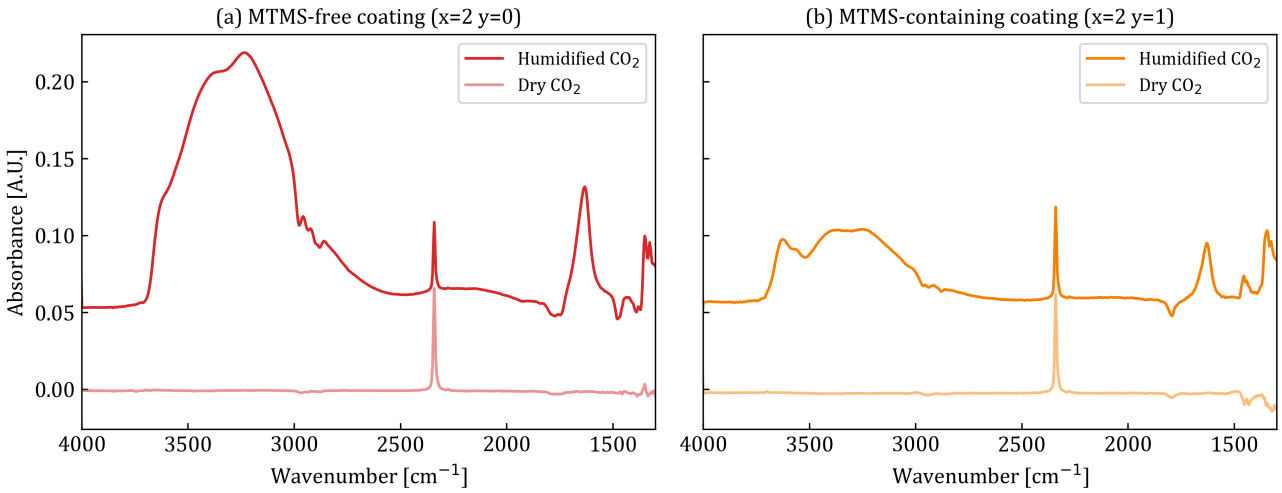

Figure 9: ATR-FTIR differential spectra for (dark) humidified CO_2 gas and (light) dry CO_2 gas with respect to a dry N_2 background for nanocomposites synthesized with and without MTMS with ionic liquid-to-SiO_2 molar ratio of x=2, and varied y MTMS-to-TEOS molar ratio. The spectra are shifted with respect to one another for readability.

The CO_2 and H_2O content in the nanocomposite coatings should remain stable over time to ensure its practical implementation as sorbent material for electrochemical CO_2 conversion. The sorption ATR-FTIR peaks were monitored for 1.5 h after humidification of the CO_2 stream, and are reported in figure 10 for MTMS-free and MTMS-containing coatings. For both samples, the CO_2 peak height did not decrease with time, thereby showing no further displacement of CO_2 with H_2O over time. The time to steady-state in the H_2O uptake provides some interesting additional insights. In absence of methyl-modification of the silica network, the peaks for water in the 3000-3700 cm^{-1} range, both for solid- and liquid-like form, keep on increasing over the 80 min time-span, exemplifying a continued water uptake. A back-of-the-envelope calculation shows that the water supply ($\simeq$ 2.4 g/min) largely exceeded the water uptake capacity of the layer ($6.4 * 10^{-4}\,g_{H_2O}$ for a 10 µm thick layer on area of the crystal), and therefore, an equilibrium could be expected much faster. In contrast, a fast response was indeed observed for the methyl-modified silica sample in figure 10(b), where little-to-no change is observed for the H_2O peak height over time. This seems to indicate that the water uptake characteristics are different for the MTMS-modified *vs.* unmodified nanocomposites. Whereas for the MTMS-modified coating water saturation is almost instant, the unmodified coating has not only a much larger water content but it takes about 80 min to saturate. Recent work by Ni et al. has demonstrated that deconvolution of the OH-stretch region in ATR-FTIR spectra can provide quantitative insight into the nature of water interactions [38], distinguishing between weakly, moderately, and strongly hydrogen-bonded species. Such an approach may offer valuable mechanistic information in future in-situ ATR-FTIR studies, particularly regarding water balance and ionic charge transport.

4.3 Final notes on the CO_2 and H_2O sorption and transport

In the previous subsections, the CO_2 and H_2O uptake behavior of the nanocomposites was presented. These results are placed into perspective in the following paragraph, using a conceptual illustration to support the interpretation. Figure 11 provides a conceptual sketch of the nanocomposite structure. On the right hand-side, a conceptual cross section of the nanocomposite is provided, highlighting the regions where CO_2 and H_2O uptake are expected. The cartoon simplifies the complex architecture of the material, which consists of a mesoporous silica matrix formed in-situ around an ionic liquid via sol-gel synthesis. Because of the ionic liquid confinement into the mesoporous silica pores, physico-chemical properties are altered compared to bulk ionic liquid behavior. For example, for these materials, a shift in ionic liquid

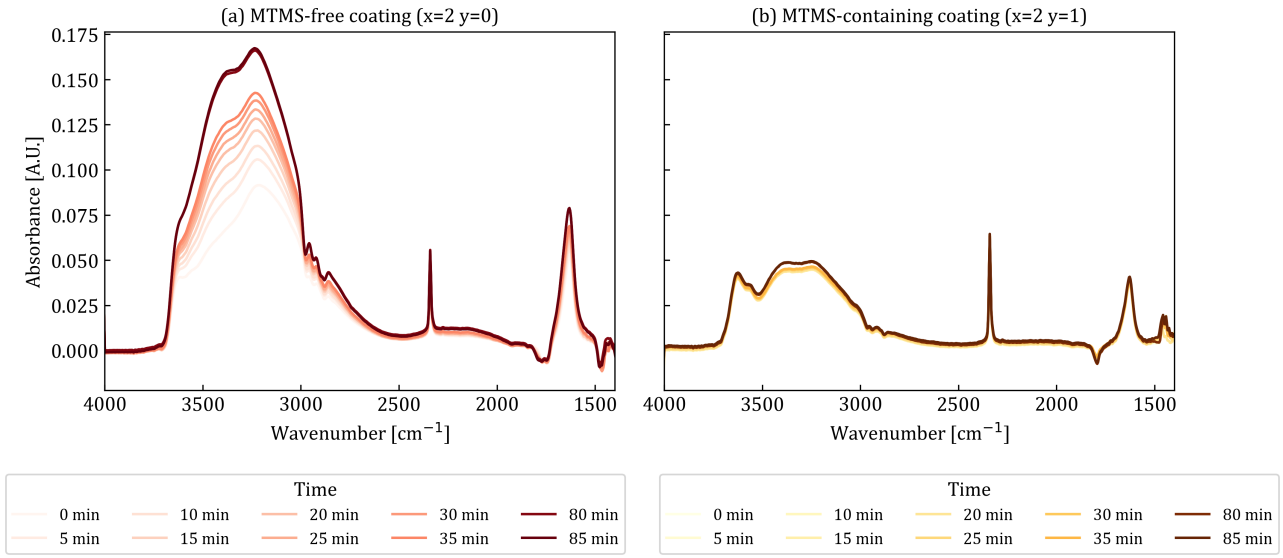

Figure 10: ATR-FTIR differential spectra at increasing time intervals after humidification of CO_2 gas (t=0 min) with respect to a dry N_2 background for nanocomposites with ionic liquid-to-SiO_2 molar ratio of x=2, and (a) y=0 mol MTMS : mol TEOS, (b) y=1 mol MTMS : mol TEOS.

melting point was previously observed [18]. Water uptake and transport can occur in both the ionic liquid (IL) and the silica phase. However, preferential uptake by the silica matrix is expected, particularly at the silica/IL interface. This is supported by ATR-FTIR spectra showing "ice-like" water signatures at the silica surface, consistent with literature reports for similar nanocomposites [39]. As such, the interfacial region is expected to be a dominant pathway for water transport. For CO_2, uptake behavior depends on the partial pressure, as explored in our previous work [18]. At low CO_2 pressures, sorption is primarily governed by the available interfacial surface area between the IL and the silica walls. This aligns with molecular simulation studies of [HMI][TFSI] confined in 2.5 nm silica slit pores, where CO_2 preferentially adsorbs near the pore walls [40]. At higher pressures ($P_{CO_2} > 0.4$ bar), uptake is increasingly influenced by bulk IL properties, suggesting two simultaneous transport mechanisms: interfacial and bulk.

The competitiveness of CO_2 and H_2O transport is therefore expected to depend on the silica wall chemistry. In particular, methyl-modification of the silica surface may reduce local H_2O uptake, thereby preserving selective CO_2 sorption sites at the interface. However, such modifications may also alter the ordering and interactions of the IL, potentially affecting the sorption mechanism.

Overall, determining the exact location and nature of sorbate uptake and transport mechanisms remains challenging due to the composite's structural complexity. While the illustrative sketch provides a conceptual framework to guide the reader's understanding, the actual distribution of CO_2, H_2O, and ionic species is likely governed by dynamic and multicomponent interactions. This complexity becomes particularly relevant when implementing the material as an electrolyte in electrochemical devices, where reactant and product transport through the nanocomposite will be influenced by coupled diffusion and competitive sorption phenomena.

Based on the available information, it is not trivial to determine which sites are dedicated to CO_2 and H_2O sorption, and which diffusion paths are taken for the individual components. It appears, however, that some competition may be found at the silica/ionic liquid interface, in-line with findings for non-methyl modified nanocomposites. The methyl-modification may enable preservation of selective CO_2 sorption sites at the interface by reducing H_2O uptake locally. However, it may also result in altered interactions and ordering of the ionic liquid anion and cation, and thus yield a different CO_2 sorption mechanism. Drawing definitive conclusions on the exact location and nature of sorbate uptake remains non-trivial. The nanocomposite structure introduces multiple layers of complexity, including interfacial ordering of ionic liquid components, pore wall chemistry, and confinement effects. These factors influence local electrostatics and coordination environments, which in turn affect sorption behavior. While the illustrative sketch

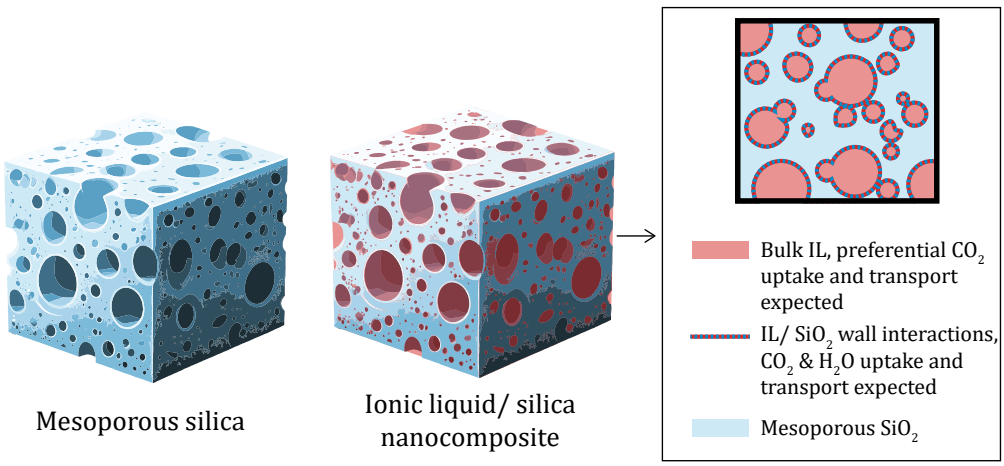

Figure 11: Conceptual illustration of the material structure and sorbate distribution. *Left:* schematic of mesoporous silica matrix for structural understanding. *Middle:* simplified representation of the nanocomposite (not to scale, the ionic liquid-filled pore volume is in reality significantly larger than shown). *Right:* cross-sectional view of the nanocomposite, showing silica, silica/ ionic liquid (IL) interfacial walls, and ionic liquid domains.

provides a conceptual framework to guide the reader's understanding, the actual distribution of CO_2, H_2O, and ionic species is likely governed by dynamic and multicomponent interactions. This complexity becomes particularly relevant when implementing the material as an electrolyte in electrochemical devices, where reactant and product transport through the nanocomposite will be influenced by coupled diffusion and competitive sorption phenomena.

5 Proof-of-concept: integrated CO_2 capture and electrochemical utilization

5.1 Ionic conductivity for multifunctional sorbent electrolyte nanocomposites

The ionic conductivity of the different composites was evaluated under varied relative humidity (5-90 %) to assess the interconnectedness of the ionic liquid-filled silica pores and the material's potential as solid electrolyte and CO_2/H_2O sorbent for electrochemical CO_2 reduction. To evaluate this, an interdigitated electrode set-up was coated with different nanocomposites via spin-coating (*cf.* Materials and Methods section). Each conductivity measurements at ambient relative humidity was performed with four different electrode finger spacings and averages are reported.

The ionic conductivity increased with relative humidity for both modified and unmodified composites (figure 12), showcasing the role of interface water in the ionic conductivity. Interestingly, the conductivity for the modified composite is within a 10 % difference of the unmodified nanocomposite. The addition of methyl groups therefore does not seem to have impacted the interconnectedness of the silica matrix. Overall, the measured ionic conductivity was in the range of values obtained for typical ionic liquids (2 mS/cm for [BMP][TFSI] at 20 °C [41]), thereby making it a suitable sorbent electrolyte for CO_2 electroreduction.

5.2 Assessment of the electrochemical CO_2 reduction

The nanocomposites were integrated as sorbent composite electrolytes onto a planar model electrochemical CO_2 reduction device with working, counter, and pseudo-reference electrodes represented in figure 13. Low current galvanostatic experiments were run for an hour for (non)methyl-functionalized sorbent composite electrolytes and products were analyzed by gas chromatography (*cf.* Materials and Methods). This simplified device was used for the proof-of-concept, with as target to demonstrate (1) that reactants and

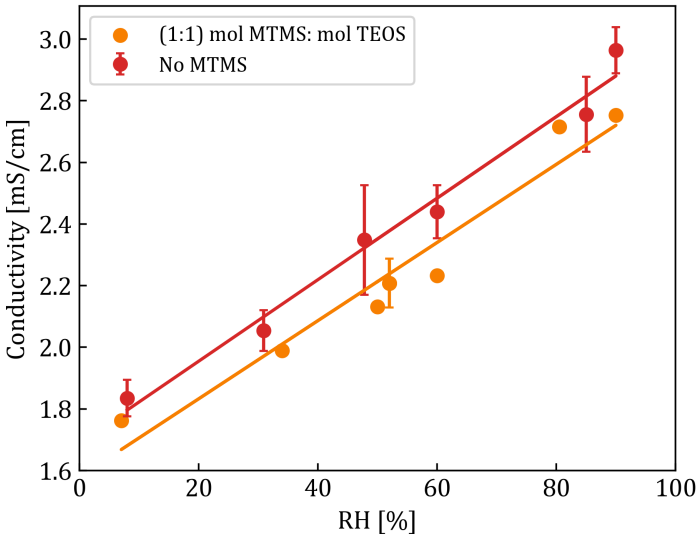

Figure 12: Ionic conductivity measured under varied relative humidity (RH) with a interdigitated electrode assembly (IDEA) for nanocomposites with [BMP][TFSI]-to-SiO_2 molar ratio of x=2, (a) y=0 mol MTMS : mol TEOS, (b) y=1 mol MTMS : mol TEOS, measured on electrodes devices with 110 µm electrode finger spacings. At ambient relative humidity, four different electrode finger spacings were used (50, 110, 170 and 230 µm), and for the MTMS-free sample, three individually coated IDEAs were tested. For these, the standard deviation is represented.

products can cross the gas/sorbent interface, (2) that the sorbent electrolyte provides ionic coupling as well as reactant and product transport from the gas phase to the catalyst and vice versa, and (3) that CO_2 and H_2O are re electrochemically utilized from the sorbed phase for the reduction reaction of CO_2 to CO (*cf.* figure 13).

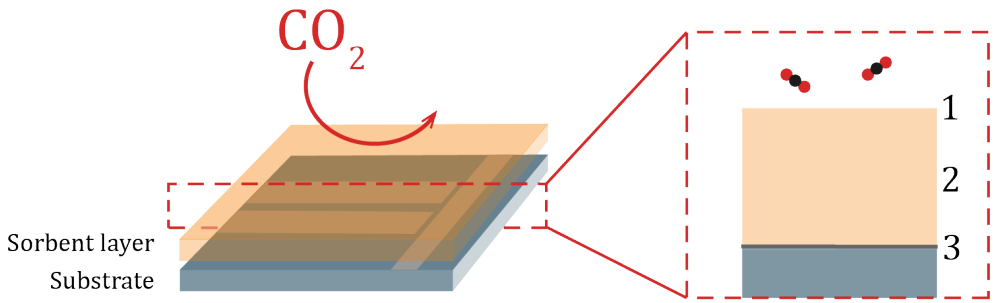

Figure 13: Illustrative sketch of the device for the CO_2 reduction proof-of-concept, composed of a non-conductive planar substrate (blue) with working (Ag)/ counter (Pt)/ pseudo-reference (Ag) electrodes (grey), coated with the sorbent nanocomposite electrolyte (orange). Three effects are studied with the device, namely (1) the capacity of the material to uptake and release CO_2, H_2O and products across the gas/ sorbent interface (2) enable CO_2, H_2O and product transport through the sorbent and (3) evidence the availability of CO_2 for electrochemical reaction at the catalyst interface.

As illustrated in figure 14, both hydrogen and carbon monoxide were produced from the (un)modified nanocomposites, thereby demonstrating the electrolytic function of the nanocomposites with and without methyl functionalization, but more importantly the CO_2 and H_2O availability for electrochemical utilization. For nanocomposites without methyl modification, hydrogen evolution was largely preferential to CO production (64:1 mol H_2/CO). However, upon methyl modification, the selectivity of the reaction switched towards CO production, leading to a 1:3 H_2:CO molar production ratio.

The authors highlight that in this work, a dedicated testing set-up was developed, with as aim to evaluate the core functionalities of the sorbent composite electrolyte: CO_2 and H_2O uptake, their electrochemical utilization from the sorbed phase, product release and ionic conductivity. This set-up is not intended to represent a practical electrolyzer for large-scale implementation or optimized performance. Instead, it

serves to isolate and study the behavior of the material under controlled conditions. The closed electrolyte layer over the electrodes, while useful to ensure product utilization for the sorbent rather than from the environment, introduces limitations in product transport and accumulation, which in turn affects the measured Faradaic efficiency. As such, the obtained total Faraday Efficiency for the tests reported in figure 14 amounts respectively 55 and 56 % for the MTMS-free and MTMS-containing sols (*cf.* SI S.5. for more information of the Faraday Efficiency). These results reflect the constraints of the test configuration rather than the intrinsic limitations of the material. Future work will focus on integrating the sorbent composite into scalable electrolyzer architectures, aiming to overcome these limitations and assess long-term performance under realistic operating conditions.

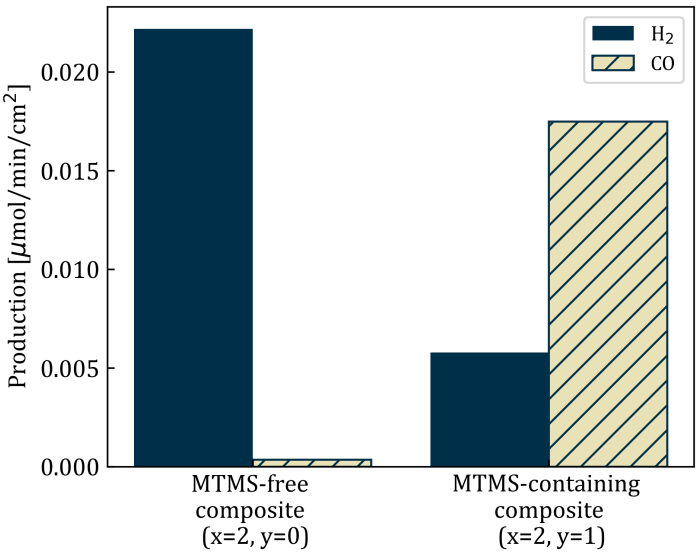

Figure 14: Product formation for electrochemical reduction in sorbent-enhanced electrolytes, namely nanocomposites with ionic liquid-to-SiO_2 molar ratio of x=2, (a) y=0 mol MTMS : mol TEOS, (b) y=1 mol MTMS : mol TEOS at 0.13 mA/cm^{-2} for 1 h.

H_2O and CO_2 electroreduction directly from a solid sorbent electrolyte was demonstrated for the first time from a gas phase stream, and selectivity towards CO_2 reduction products was steered by methyl-functionalization of the silica network. Several mechanisms might be involved in the modified electroreduction performance. Firstly, methyl-functionalization inhibited displacement of CO_2 under humid conditions, resulting in a 1.4 times increase of CO_2 concentration in the functionalized composite vs. non-functionalized composites under humid feeds (table 2). The simple concentrations difference is, however, not sufficient to explain the large selectivity change. The methyl modification might also enable improved CO_2 uptake kinetics under humidified environment. Water content, or even simply proton supply, have been shown previously to have a tremendous impact on CO_2 reduction performance, for example in Membrane Electrode Assembly electrolyzer set-ups [23, 42]. Next to proton mass transport limitations that might favor the CO_2 reduction, stabilization of intermediates at the catalyst/ sorbent composite electrolyte might play an important role in determining the process selectivity. These hypotheses are currently under investigation and will be addressed in a follow-up study focused on an optimized electrode design. This follow-up study combines experimental and modeling approaches to explore the influence of methylation on sorbent performance, including CO_2 uptake kinetics, diffusion, and reaction rates, and is expected to be published shortly.

As an additional outlook, combining molecular dynamics simulations with experimental data could provide a better understanding of influence of the catalyst/ sorbent interface effect on the CO_2 reduction reaction pathway and kinetics [43]. as such, the influence of the microscopic and macroscopic ordering of the nanocomposite could be studied, particularly regarding the trapping and stabilization of reaction intermediates. However, such modeling efforts require a sufficiently detailed understanding of the material system, for example regarding pore orientation at the catalyst/nanocomposite interface, or identification

of key intermediates using in-situ characterization techniques.

Table 2: Overview of the different sorbent composite electrolytes' sorption performance at the electrochemical reduction reaction conditions (85 % relative humidity, 0.13 mA/cm^{-2} for 1 h).

	MTMS-free sol	MTMS-containing sol
Composition (mol MTMS: mol TEOS)	0	1
H_2O uptake [mmol/g]	1	0.25
CO_2 uptake, P_{CO2} = 1 bar [mmol/g]	0.05	0.07

6 An outlook towards practical integration of the sorbent electrolyte for full gas phase CO_2 electroreduction

Integrated full gas phase CO_2 electroreduction has not been widely explored in practical electrolyzers the literature. The term *integrated full gas phase* electrolyzer is used here to refer to a system that operates without any liquid catholyte or any liquid anolyte, and that is built for high throughput performance. This typically involves membrane electrode assemblies (MEAs), where the electrodes are in close contact with the membrane and the entire cell is designed for efficient reactant and product transport while minimizing ohmic losses. The use of integrated full gas phase electrolyzers has been studied more extensively for the Hydrogen Evolution Reaction (HER) [44, 45] using cation exchange membranes (CEMs), such as Nafion [46]. A study using a comparable set-up for CO_2 reduction using a CEM showed that it is difficult to achieve good selectivity over the HER [47]. In contrast, anion exchange membranes (AEMs) have shown early promising results. For example, Dioxide materials have demonstrated a working concept [48]. However, this approach is not straightforward, and preliminary tests in our lab highlighted engineering challenges including maintaining membrane hydration. These challenges concur with the scarcity of reports for high throughput full gas phase CO_2 electroreduction (*cf.* figure 1).

Because of the above-mentioned integration challenges, it is not trivial to directly apply the novel concept presented in this work into a practical full gas phase electrolyzer. A fundamentally new cell architecture is required to test the integration of a sorbent electrolyte for CO_2 electroreduction. Figure 15b illustrates a possible upscaled configuration. This design includes porous electrodes with a large surface area, close electrode spacing to reduce ohmic losses, and a thin separator. In this concept, the sorbent material itself acts as the separator. For comparison, we briefly compare the set-up with a more conventional approach for integrated CO_2 reduction: a liquid-anolyte-operated MEA, with gas-operated cathode side (figure 15a). This differs from a fully gas phase system. Indeed, in this case, the liquid anolyte can reach the cathode through the membrane, changing the local reaction conditions.

Integrating the sorbent electrolyte into a full gas phase electrolyzer requires careful concept development and a solid understanding of the field. While some studies have implemented sorbents in high-throughput electrolyzers, the results are, in our opinion, inconclusive. Performance indeed often remains close to that of non-sorbent-modified systems [49, 50, 51]. At the same time, full gas phase CO_2 electrolyzers are still under development. Unlike hydrogen systems, vapor-fed (*i.e.,* liquid-electrolyte-free) CO_2 electrolyzers rarely reach high selectivity or long-term stability. Simply adding new materials to existing designs may not be conceptually sound. Instead, we must develop an electrolyzer that fits the sorbent electrolyte and the principles it introduces. Figure 15b shows one possible configuration that could support such integration. Future work will focus on addressing the practical challenges of integration, including hydration, gas management, and cell architecture optimization. These efforts will be essential to translate the sorbent electrolyte concept into scalable, high-throughput CO_2 electrolyzers.

7 Conclusion

One of the key paradoxes surrounding low temperature aqueous CO_2 electroreduction resides in the favored competitive Hydrogen Evolution Reaction (HER) in acidic media, and the loss of CO_2 reactant

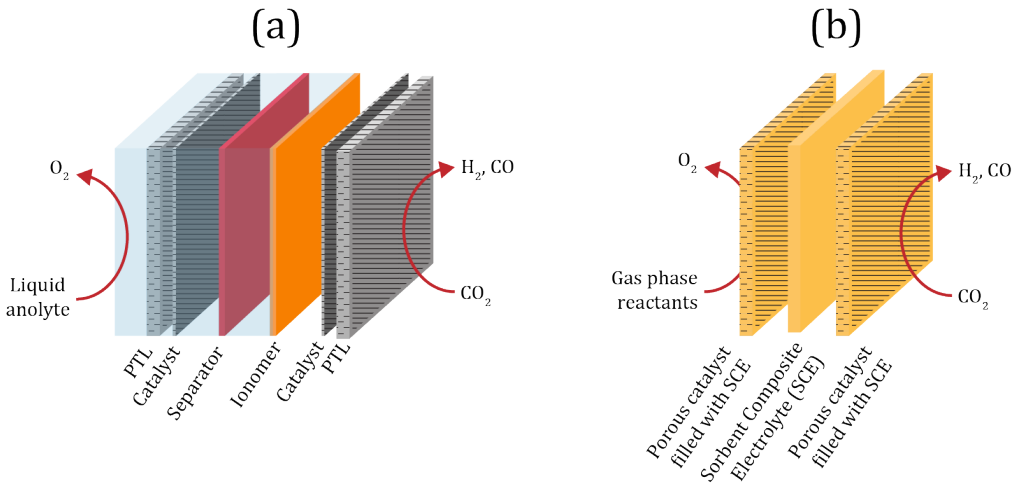

Figure 15: Illustrative sketch of (a) a gas/ liquid MEA stack for CO_2 electroreduction, with liquid anolyte and gas phase cathode feed, comprising porous transport layers (PTL), porous catalyst layers, an ionically conductive separator (*e.g.,* membrane) and ionomer (*e.g.,* the sorbent composite electrolyte (SCE)); and (b) for a fully gas-phase operated electrolyzer, with SCE serving as separator and ionomer to make ionic contact between two porous electrodes.

to the bicarbonate equilibrium in alkaline media. This study introduces a fully gas-fed electrochemical CO_2 reduction concept, enabled by the rational design of a multifunctional sorbent composite electrolyte. Transitioning to a liquid-free system eliminates diffusion limitations typically observed in MEA setups, where low CO_2-content electrolyte films hinder reactant access at the catalyst interface.

The nanocomposite material fulfills multiple roles: ensuring continuous CO_2 supply via its sorbent properties, maintaining H_2O availability through the hygroscopic nature of silica, and providing ionic conductivity for charge transport between electrodes. The in-situ functionalization of silica with methyl groups using a methyltrimethoxysilane-mediated sol-gel process enabled to tune the water uptake of the sorbent composite electrolyte without impeding CO_2 sorption. This in turn, resulted in a 50 times increase in selectivity towards CO_2 reduction in a proof-of-concept electrolysis set-up.

These results showcased the effect of rational material design to enhance CO_2 reduction by creating adequate reaction conditions at the catalyst interface. Recent research in the field of electrochemical CO_2 reduction for high Technology Readiness Level (TRL) has been focusing on MEA-based solutions. However, a thin line exists between wetting for ionic contact and flooding of the catalyst limiting reactant supply. This, in turn, has resulted in the increasing complexity of CO_2 electrolyzer designs and challenges for upscaling solutions, for example when considering pressure drops over large devices [9]. In this work, we take a step back and developed novel materials tailored to full gas-phase operation of CO_2 electrolyzers.

The proof-of-concept setup presented in this study was specifically designed to isolate and evaluate the core functionalities of the sorbent composite electrolyte:CO_2 and H_2O uptake, electrochemical utilization from the sorbed phase, product release, and ionic conductivity. Integration into a practical electrolyzer was intentionally avoided at this stage to prevent interference from other components that could obscure these fundamental assessments.

For future implementation and scalability, integrated designs resembling MEA-type cells are under investigation. Two promising configurations are being explored: figure 15(a) incorporation of the sorbent composite into a conventional MEA cell architecture, and figure 15(b) direct use of the sorbent as a functional separator between electrodes. These approaches aim to assess long-term performance, system integration, and overall efficiency, and will be the focus of follow-up studies.

8 Experimental Section

8.1 Synthesis of nanocomposites

Pellet

Tetraethyl orthosilicate (TEOS, 99 %, 86578, purchased from Sigma Aldrich), formic acid (98-100 %, 33015, purchased from Sigma Aldrich) and 1-butyl-1-methy pyrrolidinium bis(trifluoro methylsulfonyl)imide ([BMP][TFSI], 99.9 %, purchased from Solvionic S.A) were used for the sol synthesis in molar ratio $1/7.8/x$, with x the mol IL:SiO_2, varying between 0.5 and 2. For samples containing MTMS, the molar ratio x IL:SiO_2 was kept constant, but the MTMS:TEOS molar ratio y was varied between 0.25 and 1. The ionic liquid and formic acid, and separately the MTMS and TEOS, were combined in vials and mixed by manual shaking for approximately 10 seconds, until a visually homogeneous phase was observed, based on a method described previously by Vioux et al. [21]. The ionic liquid mix was added to the alkoxide solution in a sample vial, with a total solution volume kept at 3 mL for all samples. The vials were closed and kept at 25 °C in a temperature and humidity-controlled chamber (SH-641, ESPEC Corp.) for 7 days, and gelation typically occurred within 90 min. The gelated samples were dried at a reduced pressure of 80 kPa for 7 days at room temperature and subsequently for 12 h under vacuum at 25 °C. The drying process was monitored by weighing with a semi-micro balance (SM 1245Di-C, VWR). Unless stated otherwise, all samples were stored under a dry argon atmosphere until further use, the latter detailed in the material characterization section.

8.1.1 Thin film coating

Coatings were obtained by spin-coating of the aforementioned solution, followed by a drying step. Sols were prepared by following the procedure described above but using a sample volume of 2 mL in a 4 mL vial. Ageing was performed for 45-75 min in a temperature and humidity-controlled chamber at 25 °C (SH-641, ESPEC Corp.) followed by 60 min in a freezer at -25 °C for MTMS-free samples. MTMS-containing samples were aged at 25 °C for 7.5 h in a temperature and humidity-controlled chamber (SH-641, ESPEC Corp.). An overview of the precursor pre-coating thermal history depending on the composition is provided in the Supporting Information (SI) Table S.2. The length of thermal treatment was chosen based on the time to gel formation, followed experimentally by viscosity and turbidity change (SI figure S1). Spin-coating was performed immediately after removal from the freezer by casting 700 µL for 5x3 cm substrates and 500 µL for 3x3 cm wafer substrates, and spinning for 12 s at 2000 RPM with an acceleration of 1000 RPM1/s. Samples were dried for 3 h at ambient conditions first, followed by a 12 h drying step under vacuum.

8.2 Material characterization methods

8.2.1 Stability in aqueous media via TGA

To assess the stability of ionogels in water, 0.3 g of sample was immersed in 3 mL of deionized water for 24 h in Eppendorf tubes, as per the method developed by Horowitz et al. [20]. After soaking, three phases could be observed: heavier leached ionic liquid at the bottom, ionogel and excess water. The leached ionic liquid was pipetted out, and the excess water discarded. The remaining ionogel was dried on a hotplate at 85 °C and loaded for Thermo-Gravimetric Analysis (TGA). The analysis was performed using a TA Instruments 5500 Discovery under 25 mL/min N_2 flow at a heating rate of 1 °C/min. The remaining ionic liquid percentage was calculated as defined in the method by Horowitz et al. [20], summarized in the supplementary information (S.2).

8.2.2 Determination of H_2O and CO_2 uptake with TGA

The water and CO_2 (>99.998 % purity) contents in different nanocomposites were analyzed using a TA Instruments 5500 Discovery with blending Gas Delivery Module (GDM) under 25 mL/min gas flow. The

respective methods for water and CO_2 are presented below.

Water uptake: Samples were saturated with water by placing them in a closed chamber at high relative humidity (85 %) for at least 24 h. After introduction of the sample in the TGA tool, the temperature was ramped from room temperature to 150 °C under N_2 (>99.999 % purity) at 1 °C/min. The mass change was attributed to water evaporation.

Carbon dioxide uptake: The nanocomposites were stored in a dry glovebox environment until the measurement. After introduction in the TGA chamber, samples were conditioned at 110 °C for 10 h under helium to remove any water sorbed during the loading procedure. Four different steps were subsequently performed to assess the CO_2 uptake under different partial pressures (*cf.* SI S.3.1.):

1. Equilibration under He at 25 °C for 40 min,
2. Isothermal step under 10 vol% CO_2 in He at 25 °C for 30 min,
3. Isothermal step under 40 vol% CO_2 in He at 25 °C for 30 min,
4. Isothermal step under 100 vol% CO_2 at 25 °C for 30 min,

The nanocomposite was then reactivated for 15 min at 110 °C under helium. The cyclability was assessed by subsequently performing a sorption step as follows:

1. Equilibration under He at 25 °C for 20 min,
2. Isothermal step under 40 vol% CO_2 in He at 25 °C for 30 min.

An overview of the standard tests performed to support the development of the TGA methodology, along with their main outcomes, is provided in Table S5 of the Supplementary Information.

Due to the difference in density, switching gases induces a change in buoyancy force F_b (eq. (1)) on the sample-containing pan defined as eq. (2).

$$F_b = -\rho * g * V \tag{1}$$

$$\Delta F_b = F_{b,CO_2} - F_{b,He} \tag{2}$$

Two corrections were applied in order to compensate for these effects, namely a correction based on an empty pan measurement, and a correction for the sample volume, as the latter was uncorrected for in the empty pan measurement. More information on the buoyancy correction can be found in the supplementary information S.3.2.

Competitive CO_2/H_2O sorption: Samples were saturated with water by placing them in a closed chamber at high relative humidity (85 %) for at least 24 h. After introduction in the TGA chamber, samples were conditioned at 25 °C for 3 h under helium to obtain a stable baseline. Subsequently, different steps were taken to assess the CO_2 uptake depending on the water content in the composite:

1. Equilibration under He at 25 °C for 3h,
2. Isothermal step under 100 vol % CO_2 at 25 °C for 40 min (sorption step),
3. Isothermal step under 100 vol % He at 25 °C for 20 min (desorption),
4. Isothermal step under 100 vol % He at 100 °C for 20 min (water evaporation),
5. Isothermal step under 100 vol % He at 25 °C for 20 min (stabilization of the baseline)

The procedure after the 3 h equilibration step (steps 2 to 5) was repeated 6 times. A graphical overview of the method is provided in SI, figure S3. All measurements were corrected with an empty pan measurement and corrected for the sample volume as defined in S.3.2.

Ionic conductivity measurements: The ionic conductivity of the synthesized nanocomposites was measured for thin films deposited on an InterDigitated Electrode Array (IDEA), as represented in figure 16(a), and evaluated with impedance spectroscopy [52]. Each IDEA was composed of 4 sets of two-electrodes devices per wafer coupon as illustrated in figure 16(a). Each device was composed of 2 contacting pads and 11 gold interdigitated fingers. Different finger spacings were used for each respective set on the array, namely 50, 110, 170 and 230 µm. The cross-section in figure 16(b) shows the layers of the IDEA, namely an Si substrate with SiO_2 layer for insulation, with patterned electrodes (Au coated on Ti adhesion layer). The nanocomposite coating for which the ionic conductivity measurement is performed, is spin-coated on top of the IDEA. The IDEAs were prepared on 200 mm Si wafers coated with a thick insulating SiO_2 layer

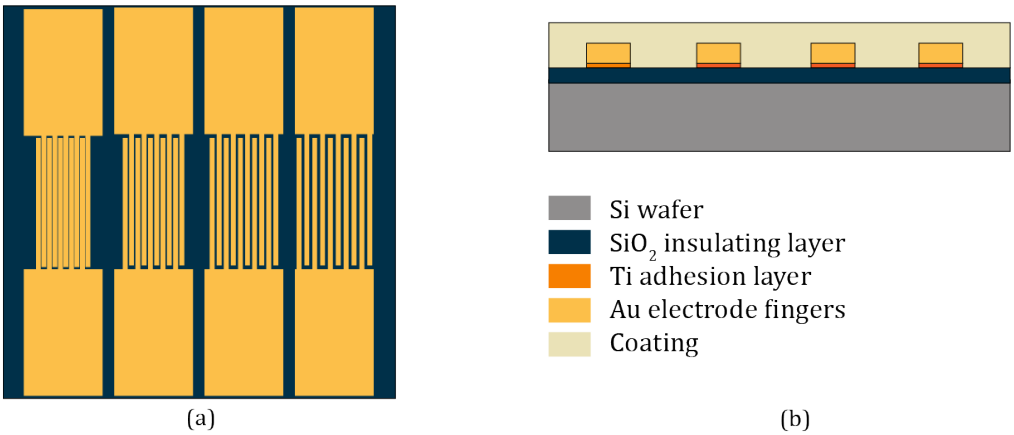

Figure 16: (a) Top view of the Interdigitated Electrode Assembly (IDEA), as applied on a 3 x 3 cm wafer coupon, showing the four two-electrodes devices with varied electrode finger spacings (50, 110, 170 and 230 µm). (b) Cross-sectional view of the IDEA, showing the substrate (750 µm), insulating SiO_2 layer (2 µm), electrode fingers (20 nm Ti, 80 nm Au) and coating for which the ionic conductivity is tested. For readability purposes, sketch (b) is not to scale.

(2 µm), on top of which a thin Ti adhesive layer (20 nm) was sputtered with a Nimbus 310 sputter tool, covered by a 80 nm sputtered gold layer using a Kurt J. Lesker LAB-18 sputter tool (step (a), figure 17). The sample was immediately transferred from one tool to the other between the depositions. An PiXDRO LP50 inkjet printer was used to draw the interdigitated electrode pattern atop the gold layer using a Sunjet U9516 hotmelt ink from SunChemicals, resistant to acids (step (b), figure 17). The metal layers on the non-ink protected regions were dissolved in two subsequent steps. First, the wafer was treated in diluted aqua regia (5:3:1 water: HCl: HNO_3 volumetric ratio of concentrated solutions) for 5 min, followed by immersion in a 2 % HF solution for 5 min to remove the metal depositions on the ink-free regions (step (c), figure 17). Finally, the commercial ink protecting the gold electrode patterns was removed by soaking and rinsing abundantly with acetone (step (d), figure 17).

The prepared IDEA substrates were spin-coated with nanocomposite using the parameters described in the thin film coating method, resulting in coverage of the gold electrode fingers (*cf.* figure 16(b)). After the coating preparation and drying, the sample was loaded into a probe station. The ionic conductivity was determined from the Nyquist plots obtained from potentiostatic impedance, as measured in a two electrode set-up using a Biologic SP-300 potentiostat with Electrochemical Impedance Spectroscopy (EIS) module, scanning from 5 MHz to 1 Hz with a sinus amplitude of 50 mV. Measurements were repeated for each of the four subsets of fingers with varied spacing in ambient air (20 °C, relative humidity (RH) 45-60 %). Subsequently, the probe chamber was placed under continuous and constant nitrogen flow (800 mL/min). The relative humidity was controlled by varying the ratio of two separate feeds, one dry and one humidified over a gas-washing bottle filled with deionized water. The relative humidity in the probe station chamber

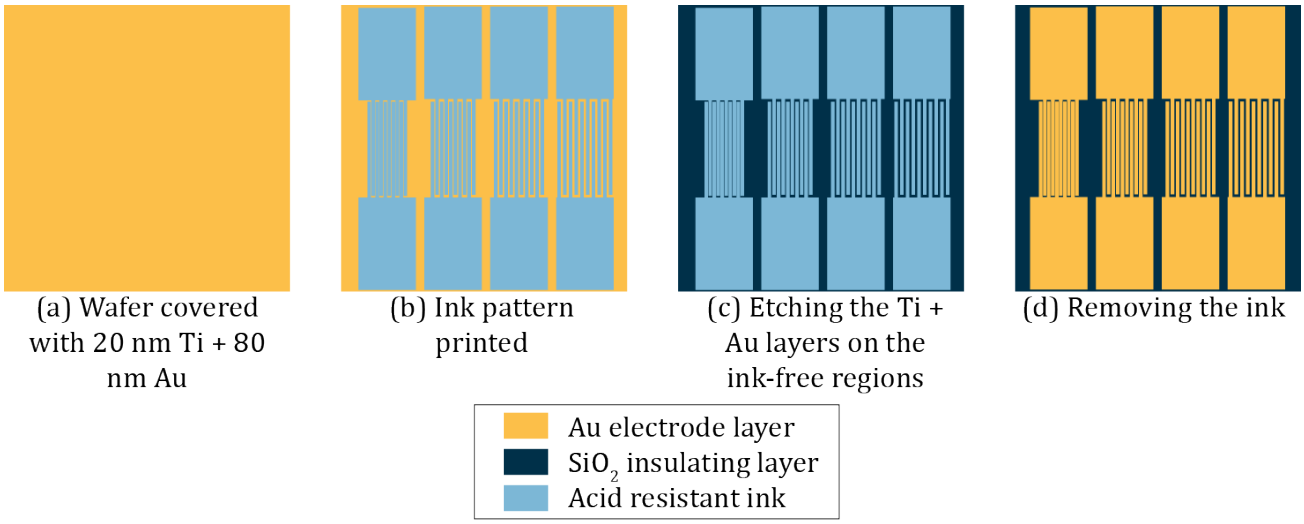

Figure 17: Processing steps for the patterning of Si/SiO_2 wafers with Ti/Au interdigitated fingers, using a chemically resistant ink for printing.

was evalutated using a Vaisala HMP7 relative humidity probe mounted in-line with the outlet flow using a DMT242SC2 sampling cell with Swagelok connectors. The relative humidity of the nitrogen stream was varied between 5-95 % and impedance measurements were done at different RH on the second subset of fingers (spacing of 110 µm). After changing the relative humidity, the EIS procedure was repeated every 2 minutes until a stable signal was obtained for the Nyquist plots. The ohmic resistance from system components R_S (*e.g.,* cables and contacts) can be read from the intercept of the semi-circle at high frequencies with the x-axis. A semi-circle was obtained at high frequencies, attributed to the resistance to ion movements, R_{ion}, and the dielectric capacitance of the nanocomposite layer. This can be fitted in an equivalent circuit, with the semi-circle accounting for the behavior of the nanocomposite layer as a series resistance (ionic resistance, R_{ion}, in parallel to a Constant Phase Element CPE_{ion}, the latter accounting for its dielectric capacitance. The resistance to ion movements, *i.e.,* the diameter of the semi-circle, was obtained by fitting the data in the EC-lab software using a R1+Q2/R2 fit, with R2 the value for R_{ion}Given the IDEA geometry, the conductivity is defined as eq. (3) with S the finger spacing, $L = 1$ cm the length of the fingers, t the thickness of the ionogel layer, R the measured resistance and N the number of fingers [52]. The thickness of the deposited layers were measured using cross-sectional Scanning Electron Microscopy (SEM) on a Philips XL30 instrument with secondary electron detector.

$$\sigma = \frac{S}{L * t * R * (N-1)} \tag{3}$$

8.3 ATR-FTIR measurements

A Nicolet 6700 FT-IR spectrometer (Thermoelectron Corporation) was used with a Smart Multi-Bounce Horizontal Attenuated Total Reflectance (HATR) accessory. The mercury-cadmium-telluride detector was cooled with liquid nitrogen prior to the experiments. Silicon crystals were prepared as substrates for the ionogel coatings. Double-side polished wafers were cut to the appropriate dimensions (5.4 cm x 3.1 cm x 775 µm) and sanded in a holder to form an isoceles trapezoid cross section with acute angles of 30°. The sloped edges were further polished with diamond sanding disks. The polished crystal was coated with the ionogel, and placed in a custom-based flow cell described by Vrancken et al. [53]. A gas flow (N_2 or CO_2) was passed above the coated substrate at a flow rate of 100 mL/min. Humidified streams were obtained by passing the feed stream over a gas-washing bottle filled with deionized water upstream of the flow cell.

The depth of penetration of the IR signal should be inferior to the coating thickness to ensure that the

signal comes from within the coating and not from above in the gas phase (*cf.* figure 18). The penetration depth was computed as eq. (4) with λ_0 the wavelength of the infrared radiation in vacuum, $n_1 = 3.4$ the refractive index of the Si ATR crystal, n_2 the refractive index of the sample and $\Theta_1 = 60^o$ the angle of incidence. The refractive index of a 390 nm film was measured with a Woollam RC2 ellipsometer and computed using an oscillator model based on angle scans between 45 and 85° with increments of 5°. A refractive index of 1.4 was obtained, in line with the expected values for pure [BMP][TFSI] (1.42) and SiO_2 (1.38). Therefore, this value was used for all samples comnpositions.

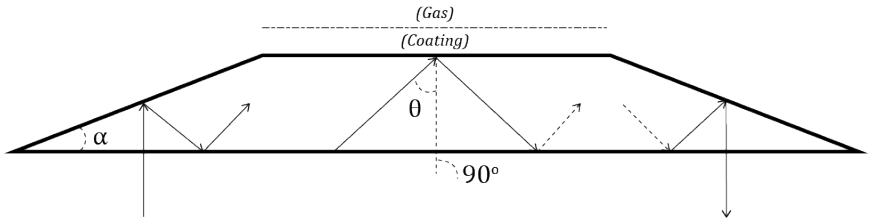

Figure 18: Illustrative sketch of the ATR-FTIR crystal and the IR beam's penetration path. The coating is applied on top, with gases introduced above it. Note that the sketch and beam path are not to scale. The angles are $\alpha = 30°$ and $\theta = 60°$, with the beam reflecting 12 times before exiting.

$$d_p = \frac{\lambda_0}{2\pi(n_1^2 \sin^2 \Theta_1 - n_2^2)^2} \tag{4}$$

The coated substrates were sealed under argon atmosphere after drying, and mounted directly into the flow cell to prevent air exposure. A reference spectrum was taken under dry nitrogen with a resolution of 4 cm^{-1} and 64 scans and subtracted from measurements under CO_2 or humidified gases. To exclude water absorption during cell assembly, a stable baseline spectrum was needed under dry conditions N_2 before starting the measurements. The cell was flushed with dry N_2 until this was achieved.

8.4 Electrochemical CO_2 reduction

To validate the concept introduced in this work, a dedicated laboratory-scale test setup was developed, as illustrated in figure 13. This setup was specifically designed to isolate and study the core functionalities of the sorbent composite electrolyte: CO_2 and H_2O uptake and uptake, their electrochemical utilization from the sorbed phase, product release, and ionic conductivity. It is important to note that this configuration does not represent a practical electrolyzer intended for large-scale implementation or optimized performance.

The simplified architecture was chosen to avoid confounding effects from complex cell designs, such as MEA systems, where complex architectures can obscure the origin of reactants and ionic conduction. For example, in such systems, it would be difficult to confirm whether CO_2 reduction occurred from the sorbent phase or from the gas-phase reactant supply, or whether water and ions originated from the sorbent or from anolyte crossover over the membrane.

In this simplified test setup, the electrodes are planar and have limited surface area, positioned in close proximity to one another. As a result, cathodic and anodic products are not physically separated, and high current densities cannot be sustained without risking physical breakage of the electrolyte layer due to excessive product formation. These constraints inherently limit the achievable Faradaic efficiency, current density, and long-term stability, making them not representative of practical electrolyzer performance benchmarks. Instead, the focus of this setup is on concept demonstration, providing a proof-of-concept for the use of solid-state sorbent electrolytes in gas-fed CO_2 electroreduction. The methodology described below outlines the fabrication and operation of this test platform.

Electrochemical tests were performed using 3 cm x 3 cm Si/SiO_2 (2 µm) substrate partially coated with a 10 nm TiW (thermal evaporation, Alcatel) and a 20 nm Ti adhesion layer for deposition of the three electrodes (0.75 cm^{-2} each). A 70 nm thick silver working electrode (WE) and pseudo-reference electrode

were deposited on top of the TiW adhesion layer (thermal evaporation, Alcatel). A 70 nm thick platinum counter electrode (CE) was deposited on top of the Ti adhesion layer using a Kurt J. Lesker LAB-18 sputter tool figure 13. The electrodes were contacted with copper tape, and the contacts were covered with Teflon tape to prevent exposure of the copper. The nanocomposite coatings were deposited via spin coating, as previously described, covering the whole substrate. A VSP BioLogic potentiostat was used in galvanostatic mode for all electrochemical measurements, together with the BioLogic EC-lab software.

Samples were loaded into a flow cell chamber. The feed gases (nitrogen and carbon dioxide) were fed into the chamber at 5 mL/min. Gases were humidified to 85 % by passing over a gas washing bottle. The cell outlet was connected to a gas chromatograph (GC) for in-line measurement of CO_2 reduction products. The GC (ThermoFisher Trace 1300, customized by Interscience, Netherlands) was used to detect CO, CH_4 and C_{2+} hydrocarbons such as C_2H_4 with a flame ionization detector (FID) connected to a methanizer and He as carrier gas. H_2 was detected with a thermal conductivity detector (TCD) using N_2 as the carrier gas. The analyzed streams are passed over micropacked ShinCarbon columns (SC-ST 100–120 0.5 m*1/16" SS) and a fused silica column (Rtx-624 30 µm 30 m*0.53 mm) to separate C_2H_4 and alcohols. The GC was calibrated using standard gas mixtures in N_2 at concentrations of 10, 100, 500 and 1000 ppm (Nippon gas). Peak integration was performed using the Chromeleon software (Thermofisher). The CO_2 conversion to products was quantified based on the measured volumetric outlet flow rate, and assuming the ideal gas law for conversion to molar flow. Conversion to Faraday efficiency was done as eq. (5), with z the number of electrons involved in the reaction, F the Faraday constant, X the amount (ppm) of product detected, ϕ_n the total outlet molar flow (mol/s) and i the passed current (A). The outlet flow was measured using a Restek ProFLOW 6000 Flowmeter. Initial tests showed constant and stable product release between 10 and 80 min of the gavanostatic experiment start. Given the focus of this work on an initial proof-of-concept, stability was not investigated beyond 80 min of operation.

$$\mathrm{FE} = \frac{z * F * X * 10^{-6} * \phi_n}{i} * 100 \tag{5}$$

Supporting Information

Supporting Information is available from the Wiley Online Library or from the author.

Acknowledgments

The authors warmly thank Frederik Hanssen and Karine Kenis for their help with hardware development. MvL gratefully acknowledges the support of the PhD fellowship (Grant No. 1SD5923N) from the Research Foundation Flanders (FWO).

References

[1] Intergovernmental Panel on Climate Change (IPCC), *Climate Change 2022 - Mitigation of Climate Change: Working Group III Contribution to the Sixth Assessment Report of the Intergovernmental Panel on Climate Change*, Cambridge University Press, **2023**.

[2] European Commission, The european green deal, `https://ec.europa.eu/info/sites/info/files/european-green-deal-communication_en.pdf`, **2019**, Accessed: 2024-10.

[3] Y. Hori, R. Takahashi, Y. Yoshinami, A. Murata, *The Journal of Physical Chemistry B* **1997**, *101*, 36 7075.

[4] Y. i. Hori, *Modern aspects of electrochemistry* **2008**, 89–189.

[5] Twelve, Twelve announces $ 645 million in funding led by TPG to transform CO_2 into jet fuel and e-chemicals at scale, `https://www.twelve.co/post/twelve-announces-645-million-in-funding-led-by-tpg-to-transform-co2-in-jet-fuel-and-e-chemicals-a-s`, **2024**, Accessed: 29/10/2024.

[6] F. P. García de Arquer, C.-T. Dinh, A. Ozden, J. Wicks, C. McCallum, A. R. Kirmani, D.-H. Nam, C. Gabardo, A. Seifitokaldani, X. Wang, et al., *Science* **2020**, *367*, 6478 661.

[7] Á. Vass, A. Kormányos, Z. Kószó, B. Endrodi, C. Janáky, *ACS catalysis* **2022**, *12*, 2 1037.

[8] A. F. Staerz, M. van Leeuwen, T. Priamushko, T. Saatkamp, B. Endrődi, N. Plankensteiner, M. Jobbagy, S. Pahlavan, M. J. Blom, C. Janáky, et al., *Angewandte Chemie International Edition* **2024**, *63*, 5 e202306503.

[9] L. M. Baumgartner, C. I. Koopman, A. Forner-Cuenca, D. A. Vermaas, *ACS sustainable chemistry & engineering* **2022**, *10*, 14 4683.

[10] D. Wakerley, S. Lamaison, J. Wicks, A. Clemens, J. Feaster, D. Corral, S. A. Jaffer, A. Sarkar, M. Fontecave, E. B. Duoss, et al., *Nature Energy* **2022**, *7*, 2 130.

[11] M. E. Leonard, L. E. Clarke, A. Forner-Cuenca, S. M. Brown, F. R. Brushett, *ChemSusChem* **2020**, *13*, 2 400.

[12] S. Hernandez-Aldave, E. Andreoli, *Catalysts* **2020**, *10*, 6 713.

[13] A. Reyes, R. P. Jansonius, B. A. Mowbray, Y. Cao, D. G. Wheeler, J. Chau, D. J. Dvorak, C. P. Berlinguette, *ACS Energy Letters* **2020**, *5*, 5 1612.

[14] J. Biemolt, J. Singh, G. Prats Vergel, H. M. Pelzer, T. Burdyny, *ACS Energy Letters* **2025**, *10* 807.

[15] E. W. Lees, J. C. Bui, O. Romiluyi, A. T. Bell, A. Z. Weber, *Nature Chemical Engineering* **2024**, *1*, 5 340.

[16] G. O. Larrazábal, P. Strøm-Hansen, J. P. Heli, K. Zeiter, K. T. Therkildsen, I. Chorkendorff, B. Seger, *ACS applied materials & interfaces* **2019**, *11*, 44 41281.

[17] K. Yang, R. Kas, W. A. Smith, *Journal of the American Chemical Society* **2019**, *141*, 40 15891.

[18] M. van Leeuwen, N. Plankensteiner, R. Maity, J. G. Loe, J. F. Denayer, R. Ameloot, P. M. Vereecken, *Microporous and Mesoporous Materials* **2024**, 113374.

[19] X. Chen, P. M. Vereecken, *Advanced Materials Interfaces* **2019**, *6*, 1 1800899.

[20] A. I. Horowitz, Y. Wang, M. J. Panzer, *Green chemistry* **2013**, *15*, 12 3414.

[21] M.-A. Néouze, J. Le Bideau, P. Gaveau, S. Bellayer, A. Vioux, *Chemistry of Materials* **2006**, *18*, 17 3931.

[22] A. Senocrate, F. Bernasconi, D. Rentsch, K. Kraft, M. Trottmann, A. Wichser, D. Bleiner, C. Battaglia, *ACS Applied Energy Materials* **2022**, *5*, 11 14504.

[23] B. Wu, B. Wang, B. Cai, C. Wu, W. W. Tjiu, M. Zhang, Z. Aabdin, S. Xi, Y. Lum, *Journal of the American Chemical Society* **2024**.

[24] J. Zhu, B. He, J. Huang, C. Li, T. Ren, *Microporous and Mesoporous Materials* **2018**, *260* 190.

[25] M. Mirzaei, A. R. Badiei, B. Mokhtarani, A. Sharifi, *Journal of Molecular Liquids* **2017**, *232* 462.

[26] Y. Uehara, D. Karami, N. Mahinpey, *Industrial & Engineering Chemistry Research* **2017**, *56*, 48 14316.

[27] G. L. Avellaneda, R. Denoyel, I. Beurroies, *Microporous and Mesoporous Materials* **2024**, *363* 112801.

[28] N. Chanut, S. Bourrelly, B. Kuchta, C. Serre, J.-S. Chang, P. A. Wright, P. L. Llewellyn, *ChemSusChem* **2017**, *10*, 7 1543.

[29] P. Carvalho, K. Kurnia, J. Coutinho, *Physical Chemistry Chemical Physics* **2016**, *18*, 22 14757.

[30] P. Innocenzi, *The sol to gel transition*, Springer, **2016**.

[31] J. A. Schott, C.-L. Do-Thanh, W. Shan, N. G. Puskar, S. Dai, S. M. Mahurin, *Green Chemical Engineering* **2021**, *2*, 4 392.

[32] J. Y. Shin, S. A. Yamada, M. D. Fayer, *Journal of the American Chemical Society* **2017**, *139*, 32 11222.

[33] T. Brinzer, E. J. Berquist, Z. Ren, S. Dutta, C. A. Johnson, C. S. Krisher, D. S. Lambrecht, S. Garrett-Roe, *The Journal of chemical physics* **2015**, *142*, 21.

[34] S. Y. Venyaminov, F. G. Prendergast, *Analytical biochemistry* **1997**, *248*, 2 234.

[35] S. Pershin, A. Bunkin, V. Lukyanchenko, R. Nigmatullin, *Laser Physics Letters* **2007**, *4*, 11 809.

[36] D. Eisenberg, W. Kauzmann, *The structure and properties of water*, Oxford University Press, USA, **2005**.

[37] G. Orcel, J. Phalippou, L. L. Hench, *Journal of non-crystalline solids* **1986**, *88*, 1 114.

[38] W. Ni, J. L. Meibom, N. U. Hassan, M. Chang, Y.-C. Chu, A. Krammer, S. Sun, Y. Zheng, L. Bai, W. Ma, et al., *Nature Catalysis* **2023**, *6*, 9 773.

[39] X. Chen, B. Put, A. Sagara, K. Gandrud, M. Murata, J. A. Steele, H. Yabe, T. Hantschel, M. Roeffaers, M. Tomiyama, et al., *Science advances* **2020**, *6*, 2 eaav3400.

[40] W. Shi, D. R. Luebke, *Langmuir* **2013**, *29*, 18 5563.

[41] Sigma-Aldrich, 1-butyl-1-methylpyrrolidinium bis(trifluoromethylsulfonyl)imide - specification sheet, `https://www.sigmaaldrich.com/US/en/specification-sheet/SIAL/40963`, **2025**, Accessed: 20/02/2025.

[42] S. Subramanian, K. Yang, M. Li, M. Sassenburg, M. Abdinejad, E. Irtem, J. Middelkoop, T. Burdyny, *ACS Energy Letters* **2022**, *8*, 1 222.

[43] Y. He, M. Wang, H. Ji, Q. Cheng, S. Liu, Y. Huan, T. Qian, C. Yan, *Advanced Functional Materials* **2025**, *35*, 3 2413703.

[44] J. Guo, Y. Zhang, A. Zavabeti, K. Chen, Y. Guo, G. Hu, X. Fan, G. K. Li, *Nature communications* **2022**, *13*, 1 5046.

[45] V. Rishikesan, S. Singh, P. M. Vereecken, *Journal of The Electrochemical Society* **2025**, *172*, 3 034509.

[46] J. M. Spurgeon, N. S. Lewis, *Energy & Environmental Science* **2011**, *4*, 8 2993.

[47] J.-B. Vennekoetter, R. Sengpiel, M. Wessling, *Chemical Engineering Journal* **2019**, *364* 89.

[48] R. B. Kutz, Q. Chen, H. Yang, S. D. Sajjad, Z. Liu, I. R. Masel, *Energy Technology* **2017**, *5*, 6 929.

[49] D.-H. Nam, O. Shekhah, A. Ozden, C. McCallum, F. Li, X. Wang, Y. Lum, T. Lee, J. Li, J. Wicks, et al., *Advanced Materials* **2022**, *34*, 51 2207088.

[50] H. Rabiee, M. Li, P. Yan, Y. Wu, X. Zhang, F. Dorosti, X. Zhang, B. Ma, S. Hu, H. Wang, et al., *Advanced Science* **2024**, *11*, 40 2402964.

[51] R. Chen, Q. Wu, J. Zhu, S. Wang, Z. Hu, J. Hu, J. Zhu, H. Zhang, B. Ye, Y. Sun, et al., *Journal of the American Chemical Society* **2025**, *147*, 9 7921.

[52] S. Hollevoet, *thesis* **2021**.

[53] N. Vrancken, S. Sergeant, G. Vereecke, G. Doumen, F. Holsteyns, H. Terryn, S. De Gendt, X. Xu, *Langmuir* **2017**, *33*, 15 3601.